An advanced magnetic resonance imaging perspective on the etiology of deep tissue injury

Running head: MRI of deep tissue injury etiology

J.L. Nelissen[1,2,*,§], W.A. Traa[3,*], H.H. de Boer[4], L. de Graaf[1], V. Mazzoli[1,5,6], C.D. Savci-Heijink [4], K. Nicolay[1,†], M. Froeling[7], D.L. Bader[3,8], A.J. Nederveen[5], C.W.J. Oomens[3], and G.J. Strijkers[2]

[1]Biomedical NMR, Biomedical Engineering, Eindhoven University of Technology, The Netherlands

[2]Biomedical Engineering and Physics, Academic Medical Center, Amsterdam, The Netherlands

[3]Soft Tissue Engineering and Mechanobiology, Biomedical Engineering, Eindhoven University of Technology, The Netherlands

[4]Department of Pathology, Academic Medical Center, Amsterdam, The Netherlands

[5]Department of Radiology and Nuclear Medicine, Academic Medical Center, Amsterdam, The Netherlands

[6]Orthopedic Research Lab, Radboud UMC, Nijmegen, The Netherlands

[7]Department of Radiology, University Medical Center Utrecht, Utrecht, The Netherlands

[8]Department of Health Sciences, University of Southampton, Southampton, United Kingdom

[*]authors contributed equally

[†]This work was dedicated to prof. dr. Klaas Nicolay, our friend, mentor, and a devoted researcher, who died on January 10, 2017. We will remember him for his great contribution to science and education in the field of biomedical NMR and his warm and inspiring personality.

[§]*Corresponding author:* Jules Laurent Nelissen, MSc, Biomedical NMR, Department of Biomedical Engineering, Eindhoven University of Technology, Eindhoven, the Netherlands, TU/e campus, Building Gemini-Zuid 3.116, Postbus 513, 5600 MB, Eindhoven, Tel: +31 40 247 3896, E-mail: j.l.nelissen@gmail.com

Author contributions: J.L.N, W.A.T, K.N., A.J.N, C.W.J.O., and G.J.S. contributed to the design of the study. J.L.N, W.A.T, L.G., V.M., and M.F. acquired and analyzed the MRI data. H.H.B and C.D.S. performed the histopathological procedures and scoring. All authors contributed to the interpretation of the data. J.L.N, W.A.T, C.W.J.O., and G.J.S. drafted the manuscript. J.L.N, W.A.T, H.H.B, L.G., V.M., C.D.S., K.N., M.F., D.L.B., A.J.N., C.W.J.O., and G.J.S. critically revised the work for important intellectual content. All authors approved the final version of the manuscript.

Abstract

Early diagnosis of deep tissue injury remains problematic due to the complicated and multi-factorial nature of damage induction, and the many processes involved in damage development and recovery. In this paper we present a comprehensive assessment of deep tissue injury development and remodeling in a rat model by multi-parametric magnetic resonance imaging (MRI) and histopathology.

The tibialis anterior muscle of rats was subjected to mechanical deformation for 2 h. Multi-parametric *in vivo* MRI, consisting of T_2, T_2*, mean diffusivity (MD), and angiography measurements, was applied before, during, and directly after indentation, as well as at several time points during a 14 days follow-up. MRI readouts were linked to histological analyses of the damaged tissue.

The results showed dynamic change in various MRI parameters, reflecting the histopathological status of the tissue during damage induction and repair. Increased T_2 corresponded with edema, muscle cell damage, and inflammation. T_2* was related to tissue perfusion, hemorrhage, and inflammation. MD increase and decrease reported on the tissue's microstructural integrity and reflected muscle degeneration, edema, as well as fibrosis. Angiography provided information on blockage of blood flow during deformation.

Our results indicate that the effects of a single damage causing event of only 2 h deformation were present up to 14 days. The initial tissue response to deformation, as observed by MRI, starts at the edge of the indentation. The quantitative MRI readouts provided distinct and complementary information on the extent, temporal evolution, and microstructural basis of deep tissue injury related muscle damage.

New & Noteworthy

We have applied a multi-parametric MRI approach linked to histopathology to characterize damage development and remodeling in a rat model of deep tissue injury. Our approach provided several

relevant insights in deep tissue injury. Response to damage, as observed by MRI, started at some distance from the deformation. Damage after a single indentation period persisted up to 14 days. The MRI parameters provided distinct and complementary information on the microstructural basis of the damage.

Keywords

skeletal muscle damage, multi-parametric magnetic resonance imaging, deep tissue injury, pressure ulcer, etiology

Introduction

A pressure ulcer is a form of tissue degeneration occurring when tissue is subjected to prolonged mechanical load, and is particularly common in subjects who are bedridden or wheelchair bound. Deep tissue injury was defined as an extraordinary sub-class to the original I-to-IV stage pressure ulcer classification system in the new 2014 international pressure ulcer guidelines (9, 25, 27, 43, 51, 77, 95). Typical for deep tissue injury is that damage formation starts under intact skin at the bone-muscle interface and may appear at the skin surface as a discolored spot or blood filled blister only in an advanced state (3). At this time treatment is problematic and the deep tissue injury therefore often progresses into a severe and difficult to heal stage III or IV ulcer (10, 93). Stage III or IV ulcers are associated with high costs (10,000 – 15,000 GBP per ulcer), reduced quality of life with wound closing times up to 155 days, and increased morbidity and mortality (17, 26, 34, 86, 88, 94, 105).

Early diagnosis of deep tissue injury represents a major problem. This is mainly due to the fact that often the damage is undetected in subjects with impaired sensitization, such as after spinal-cord injury, and only become visible at the skin surface in an advanced state. Also, there is often an inability to differentially diagnose deep tissue injury with other pathologies such as skin tear, ecchymosis, hematoma, dermatological condition, incontinence-associated dermatitis, kennedy terminal ulcer, ischemic tissue change, and venous engorgement (7, 10, 33). Several proof-of-principle studies showed that both imaging and biomarker approaches could play a role in early diagnosis of deep tissue injury but, to date, they have not been translated into a clinical setting (4, 21, 45, 54, 63, 68, 84, 87, 89, 91, 96, 102, 107). This may be partly due to the fact that the etiology of deep tissue injury is complex and still not fully understood (6, 92). An improved understanding of the etiology from the mechanisms causing initial damage to actual ulcer formation and potential recovery may provide new insights for the development of state-of-the-art early diagnosis methods.

In the last two decades a multi-scale strategy using cell-culture and animal studies, including those from the host group, advanced the understanding of deep tissue injury etiology considerably (11–15, 19, 37, 39, 40, 49, 58–61, 66, 79, 82, 90, 98, 103, 104). In particular, the use of an unique deep tissue

injury rat model, combining Magnetic Resonance Imaging (MRI) and Finite Element Analysis (FEA) methods have provided substantial new insights in the etiology of the deep tissue injury, the nature of the tissue deformation, and the major damage causing processes, including ischemia and direct deformation damage. Briefly, this model involves a controlled indentation of the tibialis anterior (TA) muscle of Brown-Norway (BN) rats inside a MRI scanner to image the damage formation processes in real-time and exploit the wide range of diagnostic MRI tools to measure essential factors, including tissue deformation, ischemia, and edema (99). By combining MRI with animal-specific FEA models local tissue strains could be estimated (19, 62, 73). This combined experimental-numerical approach made it possible to link the internal tissue deformations to damage development (64, 66).

Previous etiological research has mainly focused on the initial (within 24 h) damage causing mechanisms of deep tissue injury, including localized ischemia, reperfusion damage, impaired lymphatic drainage and direct deformation damage (20, 29, 38, 78). However, much less is known about the recovery processes and regeneration following the removal of the sustained mechanical deformation. Therefore, the goal of the present paper was to investigate damage induction as well as remodeling in the deep tissue injury rat model using a longitudinal multi-parametric MRI and histopathological approach, in order to clarify the mechanisms underpinning the complex etiology of deep tissue injury. We hypothesize that the multi-parametric MRI approach will provide a comprehensive view on deep tissue injury skeletal muscle damage and remodeling, as it is expected that deep tissue injury skeletal muscle damage will follow a precisely orchestrated biological remodeling pathway with the co-occurrence of multiple processes and overlapping characteristic phases.

Materials and Methods

Animal model and setup

A total of 53 Sprague-Dawley (SD) rats (♀, 11 to 13-week-old, Charles River, Paris, France) and 6 Brown-Norway (BN) rats (♀, 11-week-old, Charles River, Paris, France) were used. Animals were housed under standard laboratory conditions with a 12 h light/dark cycle and were maintained on a standard diet and with access to water *ad libitum*. The animals were divided into 6 experimental groups (Table 1) to obtain various non-invasive *in vivo* MRI estimations of damage development and remodeling as well as *ex vivo* histology up to 14 days after damage induction. For comparison with previous work, a small number of Brown-Norway rats was included in group I. All groups received MRI pre, during, and post damage inducing deformation of the TA muscle at day 0. Group III, group IV & V, and group VI were followed up for 3, 5, and 14 days, respectively.

For MRI, the rat was placed in supine position and anesthetized with isoflurane (4.0 vol% for induction, 1.0-2.0 vol% for maintenance) in 0.6 L/min medical air. Buprenorphine (0.05 mg/kg s.c.) was administered for analgesia. Eye ointment was applied to prevent eye dehydration. Body temperature was maintained at 35-37 ^{o}C with a heating blanket and monitored with a rectal temperature sensor. Respiration was monitored with a balloon pressure sensor placed on the abdomen and maintained in a physiological range by adjusting the anesthesia. The right leg of the rat was shaved and positioned in a u-shaped profile filled with alginate molding substance for firm fixation and susceptibility matching. The TA muscle in the hindleg of the rat was compressed by the indentor for 2 h. The indentor was pushed manually into the TA muscle and varied intentionally in depth and angle between animals. The indentor setup is MRI compatible, which facilitates MRI measurements during compression and injury development (74). The indentor is hollow and filled with an aqueous solution of 1 g/l $CuSO_4$, which enables precise localization of the indentor on MRI. No signs of skin surface wounds or pain were observed at any time-point. At day 0 (n = 20), day 3 (n = 6), day 5 (n = 24), and day 14 (n = 9) rats were sacrificed by means of exsanguination from the inferior vena cava.

This procedure was performed under anesthesia and after administration of analgesia. Both deformed and control TA muscles were dissected and stored for histopathological analysis.

All animal experiments were approved by the Animal Care and Use Committee of Maastricht University, Maastricht, The Netherlands (protocol 2013-047, Maastricht University, Maastricht, The Netherlands) and performed in accordance with the Directive 2010/63/EU for animal experiments of the European Union.

Multi-parametric MRI protocol

Measurements were performed with a 7.0 T small-animal MRI scanner (ParaVision 5.1, AVANCE III, Bruker BioSpin MRI GmbH, Ettlingen, Germany) equipped with a 660 mT/m, 4570 T/m/s gradient coil (BGA-12S HP, Bruker BioSpin MRI GmbH, Ettlingen, Germany). An 86-mm-inner-diameter quadrature transmit coil was used in combination with a 20-mm-diameter surface receive coil (Bruker BioSpin MRI GmbH, Ettlingen, Germany) placed on top of the TA muscle inside the indentation rod. The multi-parametric protocol consisted of T_2-weighted MRI, quantitative T_2 and T_2*-mapping, diffusion weighted imaging (DWI), and time-of-flight (TOF) MR Angiography (MRA). As indicated in table 1 the protocol differed between groups. In all groups the protocol was repeated several times during and post indentation at day 0. At the other time points the protocol was acquired only once.

T_2-weighted images were acquired with a 2D multi-slice multi-echo (MSME) sequence in axial orientation. The TA muscle was imaged by 20, 1-mm-thick slices with field of view (FOV) = 25 x 25 mm^2, a 256 x 256 reconstruction matrix (MTX) with 33% zero filling, and repetition time (TR) = 2500 ms. A total of 12 echoes were measured for which the last 10 consecutive echo times (TEs) were accumulated to obtain images with an effective echo time (TE_{eff}) of 65 ms. Chemical-shift selective (CHESS) fat suppression was used. CHESS fat suppression was visibly sufficient in these small laboratory animals with very little subcutaneous fat. Acquisition time was 8 min. In group VI T_2-weighted MRI was performed with a 2D Rapid Imaging with Refocused Echoes (RARE) sequence with higher resolution and similar T_2-weighting. Other acquisition parameters were: 16 axial slices of

1 mm, FOV = 40 x 40 mm^2, MTX = 512 x 512, number of averages (NEX) = 5, RARE factor = 8, TE_{eff} = 40 ms, TR = 2500 ms, CHESS fat suppression, and acquisition time 13 min.

T_2 quantification was performed with a 2D MSME sequence. Sequence parameters for axial slices were: number of slices = 16 or 20 of 1 mm thickness, FOV = 25 x 25 mm^2, MTX = 256 x 256, 33% zero filling, 26 equally spaced echoes (TE = 6.95 – 180.7 ms), TR = 3200 ms, CHESS fat suppression, and acquisition time ≈ 10 min. Coronal slices were acquired for groups II, III, IV, and VI. In the coronal orientation, sequence parameters were: number of slices = 6 to 20 of 1 mm thickness, FOV = 60 x 30 mm^2, MTX = 512 x 256, 33% zero filling, 20 echoes (TE = 10.18 – 203.5 ms), TR = 3200 ms, CHESS fat suppression, and acquisition time ≈ 10 min.

T_2* quantification was performed with a 2D Multi Gradient Echo (MGE) sequence. Sequence parameters in axial orientation were: number of slices = 16 or 20 of 1 mm thickness, FOV = 25 x 25 mm^2, MTX = 256 x 256, 33% zero filling, 21 echoes (TE_1 = 3.34 ms, ΔTE = 3.55 ms, TE_{21} = 74.39 ms), TR = 1350 ms, CHESS fat suppression, and acquisition time ≈ 4 min. Coronal slices were acquired for groups III, IV and VI. In coronal orientation sequence parameters were: number of slices = 6 to 20 of 1 mm thickness, FOV = 60 x 30 mm^2, MTX = 512 x 256, 33% zero filling, 12 echoes (TE_1 = 4.77 ms, ΔTE = 6.37 ms, TE_{12} = 74.83 ms), TR = 1350 ms, CHESS fat suppression, and acquisition time ≈ 4 min.

The DWI acquisition was measured with diffusion-encoding gradients applied in 3-orthogonal directions with a multi-shot Spin Echo (SE) DWI Echo Planar Imaging (EPI) sequence in 16 axial slices of 1 mm thickness. Other sequence parameters were: FOV = 60 x 30 mm^2, MTX = 128 x 64, diffusion gradient duration (δ) = 2.5 ms, diffusion gradient separation (Δ) = 10 ms, b-values = 0-2-5-10-15-20-25-50-100-200-400-600-800 s/mm^2, TE = 18 ms, TR = 4 s, NEX = 2, number of EPI segments = 4, CHESS fat suppression, and acquisition time ≈ 20 min.

MRA was performed with a TOF 2D Fast Low Angle Shot (FLASH) sequence, with the following sequence parameters: 120 slices of 0.4 mm thickness with 0.25 interslice distance, FOV = 40 x 40

194 mm^2, MTX = 256 x 256, 33% zero filling, TE = 3.8 ms, TR = 15 ms, flip angle = 80^0, and acquisition
195 time ≈ 6 min.

196 MRI data analysis

197 T_2-weighted images were scored by an MR expert for the location of hyper intensity, distal or
198 proximal, with respect to the indentor, during and after deformation of the TA muscle at day 0.

199 Quantitative T_2-maps were obtained by pixel-wise fitting the MR signal to $S(TE) = S(0)e^{-TE/T_2}$
200 (Mathematica 10, Wolfram Research, Champaign, USA). Pixels with $R^2 < 0.9$ were excluded from
201 subsequent analysis. Region-of-interest (ROI) based analysis of the axial T_2 maps was performed
202 (Matlab R2016a, The Mathworks, Inc., Natick, Massachusetts, USA). An ROI was defined by
203 manually outlining the TA muscle in all slices of the first echo of the T_2-mapping dataset (ITK –
204 SNAP, PICSL, University of Pennsylvania, USA (108)). Mean T_2 of the whole TA was determined at
205 all time points.

206 Quantitative T_2*-maps were calculated by pixel-wise fitting the MR signal to $S(TE) = S(0)e^{-TE/T_2^*}$
207 (Mathematica 10, Wolfram Research, Champaign, USA). Pixels with $R^2 < 0.9$ were excluded. ROI
208 based analysis of the axial T_2* maps was performed in Matlab. Mean T_2* of the whole TA was
209 determined at all time points as well.

210 DWI images were registered using affine translation to the first echo of the T_2-maps, followed by
211 calculation of the mean diffusivity (MD) of the averaged orthogonal directions by fitting the MR
212 signal to $\frac{S(b)}{S(0)} = e^{-b\,MD}$. All DWI data processing was performed using the open source DTItools add-
213 on for Mathematica, developed by Froeling *et al.* (36). ROI based analysis of the MD-maps was also
214 performed in Matlab. Mean MD using the same segmentation of the quantitative T_2-data of the whole
215 TA was determined at all time points.

216 The MRAs were processed by visualizing maximum intensity projections (MIPs) in OsiriX (Pixmeo
217 SARL, Geneva, Switzerland). MRA MIPs were visually inspected and assessed by an MR expert for

presence of reduced flow in the saphenous artery during indentation and increased flow in the TA compartment at day 0.

Statistical analysis

Statistical analysis was performed with the R environment for statistical computing and graphics (R Version 3.4.1, The R Foundation for Statistical Computing, Vienna, Austria). One-way repeated measure ANOVA with a Dunnett's *post hoc* test was used for comparing changes in mean T_2, T_2^*, and MD-values of the ROI over time compared to baseline, provided that the assumptions of normality and heteroscedasticity hold. Normality was assessed graphically for small sample sizes ($n < 15$). For larger sample sizes normality was assessed both graphically and by performing a Shapiro-Wilk test. Heteroscedasticity was assessed with Levene's test. If both the assumptions of normality and heteroscedasticity held Mauchly's test was used to assess sphericity and test statistics were corrected with Greenhouse-Geisser when appropriate. When the assumptions of normality and heteroscedasticity were violated the Friedman Rank Sum test with Dunnetts *post hoc* test was used.

Statistics were performed both for the data on day 0 for all groups and all six time points up to day 14 for group VI. At day 0, multiple T_2*, T_2, and MD-scans were made during the 2 h deformation period. To assess temporal changes and to prevent excessive filtering of the data due to balancing, the 2 h deformation period was divided into 2 time windows and any missing data from either window were excluded from statistical analysis. This resulted in a total of 16 animals for T_2^*, 42 animals for T_2, and 9 for MD.

Histology

For a subset of animals from groups I (BN n = 4, SD n = 4), II (n = 4), III (n = 4), IV (n = 4), and VI (n = 4) the TA muscles were transversally cut at 1 mm intervals and embedded in total in paraffin blocks. Both injured and contralateral control TA muscles were processed. From each block two 8 µm thick

histological slides were prepared; one was stained with Hematoxylin and Eosin (H&E), the other with Masson Trichrome (TRI). Blinded pathological evaluation was performed by an experienced pathologist, largely using the method as described by Hammers *et al.* (46). For this, TA muscle sections were semi-quantitatively assessed for the presence of various features of cellular damage and inflammatory response. The assessment focused on degeneration, necrosis, edema, hemorrhage, fibrosis and the presence of three groups of inflammatory cell types (neutrophils, lymphocytes/plasma cells and macrophages). Degeneration and necrosis represent a continuum of myocyte damage, with degenerative myofibers showing swelling, loss of contact with adjacent myofibers, and intracellular or directly adjacent inflammatory cells. Necrotic myocytes show more pronounced histomorphological changes with homogenization, eosinophilia and fragmentation of the cytoplasm, and pyknosis or loss of myocyte nuclei. Edema was defined as the presence of an expanded non-cellular interstitium, hemorrhage was defined as the extravasation of erythrocytes, and fibrosis was evaluated by assessing the presence of collagen deposition. Differentiation between the groups of inflammatory cells was done on the basis of nuclear and cellular morphology. The presence/severity of all features were scored on a 5-point semi-quantitative scale (none, minimal, mild, moderate, severe). In addition, the area of degeneration was scored on a 4-point scale (0-5%; 5-20%; 20-40%; >40%). Scoring was recorded on standardized scoring sheets. One-sided Wilcoxon signed rank tests with Pratt method for ties correction were used to assess changes in histopathological scoring values of all injured TA muscle sections of all different groups compared to contralateral control TA muscle sections. Correlation of histopathological scoring values to the multi-parametric MRI readouts was performed with a Spearman's rank correlation test with Bonferroni type adjustment to determine the Spearman correlation coefficient ρ. Correlation of histopathological scoring values to MD could not be determined for several scored histopathological features, due to the limited spread of the data, small number of animals, and few time-points. Histological sections were not registered to the MRI data.

Results

Multi-parametric MRI

T_2-weighted MRI was used as the principal parameter for identifying edema, damage, and inflammation caused by the 2 h loading period. Representative T_2-weighted MR images of a central, distal, and proximal slice, acquired pre, during, and post 2 h deformation are shown in Figure 1. In the central slice pre indentation the TA muscle and tibia bone are indicated by an arrow. During the indentation the indentor is clearly visible. Post deformation a large portion of the TA muscle demonstrated high intensity textured regions resembling an epi-, peri-mysium-like structure. During indentation the extensor digitorum longus (EDL) muscle also demonstrated high intensity distal to the center of indentation. By contrast, proximal to the indentation axis no evidence of high intensity was observed. Post deformation the high intensity regions in the EDL largely disappeared, with the exception of small areas located at the edge of this muscle.

Scoring for the location of the high intensity signals, *i.e.* distal or proximal with respect to the indentor, during and after deformation of the TA muscle at day 0 in T_2-weighted images of group I, V, and VI, revealed enhanced incidence distally during indentation. Of the 29 scored animals high intensity regions were demonstrated in 16 animals distally, 1 animal proximally, 7 animals distally as well as proximally, while 5 animals displayed no high intensity regions during indentation. Indeed, all but one animal with observed high intensity signals during indentation, displayed distal and/or proximal high intensity signals after indentation (see Figure 2). In 2 of the 5 animals no high intensity signals were demonstrated both during deformation and then following load release.

Quantitative water T_2-values were used to longitudinally assess the damage and remodeling processes. To illustrate damage development during indentation, Figure 3 shows representative axial and coronal T_2-maps equally spaced over the 2 h deformation period, for one selected animal pre, during, and immediately after indentation at day 0. During indentation, an increasing area with elevated T_2 was observed, starting in the EDL distally to the center of deformation (region indicated by the number 1),

and subsequently expanding in the TA muscle (region 2). Towards the end of the deformation period, elevated T_2-values were also observed proximally in the TA (region 3). In the images, the elevated T_2-areas display a stripe-like texture that appears to align with the muscle fiber architecture and the epi-perimysial structure (similar to Figure 1). Post indentation, elevated T_2-values were observed in the larger part of the TA (region 4). The elevated stripe-like texture in the coronal orientation post deformation showed interruptions near the axis of indentation. The TA muscle did not completely recover its shape following load release with a residual indentation visible.

A side-by-side comparison of axial and coronal T_2 and T_2*-maps, pre and post indentation at day 0, of the same animal as in Figure 3 (separate slice location) is shown in Figure 4. In the region of elevated T_2 and T_2*, a central region with lower T_2 and T_2* was observed (arrow). In particular, T_2*-values were lower when compared to corresponding baseline values.

A multi-parametric evaluation of the model during the full time-course of damage induction and recovery for one animal from group VI is presented in Figure 5. Images at day 0 were from healthy muscle pre-indentation to which all other time points are compared. Similar to the example shown in Figure 1, indentation caused high intensity signals on T_2-weighted images in the TA muscle body as well as between muscle and skin, which persisted up to 7 days after induction of the muscle damage. In some animals, low intensity spots were observed in the TA on days 10 and 14. The T_2-maps shown in the second row of Figure 5 display a similar time course of recovery with normalization of TA T_2-values 10 days after induction of the damage.

T_2*-maps during and post deformation at day 0 (row 3 of Figure 5) suffered from some signal loss due to field inhomogeneities caused by the indentor and because the susceptibility-matching alginate had to be partly removed to allow indentor access. At day 3 an area with elevated T_2*-values was observed in the TA, which was considerably smaller than the regions of elevated T_2. At days 5 to 14, during the remodeling phase of the damage, reduced T_2*-values were observed in most regions of the TA muscle. The MD-maps, shown in row 4, also suffered from some susceptibility-related artifacts during indentation adjacent to the position of the indentor. At day 0 directly after indentation, MD was

elevated in the TA. MD-values decreased towards day 5 to below baseline values. At day 14, MD-values in the TA were almost returned to baseline, but some regions with lower MD could still be observed. Regions of reduced MD and T_2* at day 5, 7, 10, and 14, visually co-localized with each other.

Coronal MIPs of the TOF MRA for two animals (RAT-005 and RAT-007) of group VI are shown in Figure 6. The MRA MIPs reveal the larger blood arteries in the lower leg of the rat, which can be used to assess whether major arteries are blocked by the compression. During indentation, the hollow $CuSO_4$-solution-filled indenter is also visible in the MIP (orange arrows). For RAT-007, a reduced flow in the saphenous artery was observed under indentation (blue arrow). Directly after deformation at day 0 blood flow through the saphenous artery was restored, accompanied by what appeared to be a hyperemic response in the TA compartment region (green arrow). RAT-005 did not show a reduced flow in the saphenous artery under indentation and showed only a minor hyperemic response at day 0 post. Angiograms at later days appeared normal for this animal. A movie of rotating MIPs of both animals up to 14 days is provided in the supplemental content (Supplemental Content 1). Individual time-courses of the mean parametric values of RAT-005 and RAT-007 are also shown in Figure 8. Visual assessment of the MIPs of 33 animals revealed reduced flow in a major artery, predominantly the saphenous artery in 11 animals under indentation and a hyperemic response in 20 animals at day 0 directly after deformation.

The extent and severity of damage caused by indentation of the TA and the time-course of recovery is variable between animals dependent on various factors, including the individual rat leg anatomy, the amount and angle of indentation, the induced strain in the muscle, as well as the extent of ischemia. TA muscle T_2, T_2*, and MD-values for all animals over time is presented in Figure 7. Each open circle represents a data point for a single animal at given time point, whereas the thick solid lines represent the mean parametric values for all animals at the different time points pre, during, and post indentation. It is evident that these mean values reflect the same time-course of trends observed with the single animal shown in Figure 5. Individual time-courses of the 9 animals of group VI which were followed up to 14 days are shown in Figure 8.

A detailed summary of all parametric values for all time points with the associated statistical results are presented in Table 2. T_2-values were significantly elevated compared to baseline at all timepoints. T_2* showed significantly reduced values during indentation and was significantly elevated at day 0 post and day 3. MD was significantly elevated at day 0 post, whereas at days 5 and 10 the values were significantly lower than baseline values.

It should again be noted that not all animals followed the same trends with time. As an example, two distinctly different responses are highlighted with green and magenta circles in Figure 7. The quantitative parameter maps of these two animals are presented in Figure 9. In one of these rats (magenta data points) injury from indentation was relatively mild, with T_2 and T_2*-values not different from baseline and a minimal decrease in MD at day 5. By contrast, indentation in the other animal (green data points) resulted in extensive damage in the TA muscle, with increased T_2 in the whole TA, a transient increase in both T_2* and MD shortly after indentation, followed by a persistent decrease in these values.

Histopathological evaluation

Table 3 summarizes the scorings of the histopathological evaluation. At day 0, approximately 2 hrs after indentation, TA muscle tissue was only characterized by mild edema and, in some cases, early neutrophilic infiltration. At days 3 and 5 virtually all parameters reached maximum values, corresponding with moderate to severe degeneration affecting more than 40% of the slide area. Both time-points clearly represent a different phase of the muscle damage and remodeling pathway. The high-rated pathological features, represented by moderate to severe necrosis, edema, hemorrhage, neutrophils and lymphocytes/plasma cells at day 3 are characteristics of the pro-inflammatory phase. All high-rated pathological features of day 3 were reduced to the minimal-mild level at day 5, accompanied by an increase in the number of macrophages and amount of fibrosis typical of the anti-inflammatory and remodeling phases. At day 14 the inflammation markers decreased to normal/minimal levels with, in some specimens the presence of mild fibrosis, an indication for continued remodeling of the muscle.

In Figure 10, representative H&E and TRI histological sections are depicted adjacent to the various multi-parametric MRI parameters at day 0, 3, 5, and 14. For day 14, the series of two animals are shown, one displaying mild damage (RAT-005) and one with severe damage (RAT-006). Individual time-courses of the mean parametric values of both rats are shown in Figure 8.

Distinct differences between healthy controls and injured muscle were apparent. The control sections (bottom row) showed normal muscle cells with small interstitial spaces. The edema, swollen cells, and infiltrated neutrophils observed at day 0 after indentation is in concordance with the typical epi-perimysium-like texture of elevated T_2-values and high intensity signals that were found in the T_2-maps and T_2-weighted images. The pro-inflammatory response on day 3, i.e. hemorrhage, inflammation, necrosis, and edema corresponded with diffuse elevated T_2-values on the T_2-map, whereas the T_2*-map showed areas with both elevated as well as decreased T_2*. On day 5, the parametric maps of this particular animal showed a band-like pattern with slightly elevated T_2 and reduced T_2*. This corresponded on the histology to light collagen deposition, multiple little hemorrhages, newly formed muscle cells, and numerous macrophages. Edema, necrosis, and the more pro-inflammatory neutrophils and lymphocytes were reduced in number when compared to day 3.

Even at day 14, the TA muscle tissue was not fully recovered, showing numerous small muscle cells with centrally placed nuclei and an aberrant muscle shape. This was in agreement with MRI findings, particularly for the animals with severe damage (RAT-006), which displayed collagen deposition and the presence of macrophages. However, also in the mildly damaged (RAT-005) animal, muscle tissue was not fully remodelled.

Table 4 shows the Spearman correlation coefficient ρ for the correlation of the multi-parametric MRI readouts and histopathological scoring. T_2 correlated significantly with all scored pathological features, with a strong correlation ($\rho \geq 0.80$) to degeneration area, edema, and neutrophils. Correlation of T_2 with fibrosis showed significantly weak ($\rho = 0.43$) correlation. T_2* was strongly correlated ($\rho \geq 0.80$) to necrosis, edema, hemorrhage, and neutrophils. For MD no significant correlations with pathological features were found.

Discussion

Multi-parametric MRI was applied to characterize tissue damage and remodeling in a rat model of deep tissue injury. MRI provided a macroscopic *in vivo* view of the induced damage, whereas histopathology provided the link to muscle pathology at the microscopic level. Taken together, this study highlights a number of features with respect to MR imaging biomarkers of muscle damage and regeneration which reflect the time course of deep tissue injury, as shown schematically in Figure 11.

The major established muscle damage causing mechanisms for deep tissue injury are direct deformation and ischemia. As previously reviewed by Oomens *et al.* both damage mechanisms have different features in terms of time scale and deformation threshold levels (78). Ischemic damage is a relative slow process (2 - 4 h) occurring with low levels of deformation, and is mechanistically explained by occlusion of blood and lymph vessels resulting in a change in metabolism followed by accumulation of waste products and associated decrease in local pH (37, 64, 100). By contrast, direct deformation damage can develop rapidly (≈ 10 min) in case of high levels of deformation and is a consequence of cell membrane failure and, potentially, rupture of the cytoskeleton (19, 66). In addition, impaired lymphatic drainage and reperfusion injury after load release can aggravate the damage (5, 28, 47, 49, 55, 64, 71, 85).

The skeletal muscle responded following a precisely orchestrated pathway as known from other types of acute muscle damage (contusion, laceration/puncture, strain, myotoxin, contraction-induced injury, crush injury) (8, 22–24, 52, 67, 69, 106). The onset of skeletal muscle damage was characterized by swollen and disrupted muscle fibers, increased interstitial space, edema, hemorrhages, and the first signs of inflammation with the presence of neutrophils. This was subsequently followed by the pro-inflammatory phase with significant necrosis, hemorrhages, edema, and inflammatory cell reaction of neutrophils, pro-inflammatory macrophages, and lymphocytes. Thereafter the anti-inflammatory phase is associated with the invasion of anti-inflammatory components to the damaged muscle, fibrillar collagen extracellular matrix (ECM) deposition, and first signs of myogenesis. Finally, the tissue entered a remodeling phase, partly overlapping with the anti-inflammatory phase, in which

differentiated myocytes are evident with ECM reorganization and newly formed myocytes with central nuclei.

From a diagnostic imaging perspective, there is no unique single MRI parameter which can reflect all the relevant pathological processes. We therefore employed a multi-parametric imaging approach. This strategy has been increasingly adopted in MRI to improve the overall diagnostic power (1, 16, 18, 32, 35, 41, 47, 53, 57, 64, 65, 72, 81, 90, 100, 109). In the present study, quantitative T_2, T_2*, MD have been acquired in conjunction with qualitative TOF angiography as parameters which reflect edema and inflammation, hemorrhage, tissue integrity / cellularity, and blood flow, respectively.

Tissue water T_2 is the most commonly used muscle MRI quantitative damage biomarker (48, 70). Although changes in T_2 can be caused by several pathological processes, including inflammation, necrosis, and edema, in the context of acute muscle damage it provides a parameter which reflects the severity and extent of the induced muscle damage (64–66, 97, 100). We used a higher MRI field strength and improved hardware, incorporating a surface receiver coil, which allowed for imaging T_2 with higher resolution and signal-to-noise ratio (SNR) when compared to previous studies from the host group (74, 99). This improvement resulted in the detection of elevated T_2 in an epi- and perimysial structure. We observed distal T_2 increases during the process of deformation, which supports previous observations describing distal T_2 increase directly after indentation (97). Additionally, distal T_2 increases were detected in the EDL muscle in a subset of the animals, which disappeared after load release in some of these animals. It is proposed that the distal T_2 increase is caused by edema as a result of impaired lymphatic drainage and reduced venous return in the distal parts of TA compartment.

Similar to previous findings a local T_2 increase directly under the indentor was absent during deformation (92). Indeed edema buildup is likely prevented during indentation due to the compression of the tissue. T_2 increased first distally and later both distally and proximally with respect to the indentor position but not at the axis of indentation. This shows that the effects of sustained mechanically loading on muscle can manifest itself over an area which extends beyond the site of

448 loading. Histopathology confirmed that elevated T_2-values shortly after load release were the result of
449 edema along the TA and EDL muscle fibers. At later time points, histopathology revealed extensive
450 necrosis, inflammation and, to a lesser extent, fibrosis. TA T_2-values were at a maximum between 3-5
451 days after induction of damage at the height of the inflammatory response, after which T_2-values
452 resolved (in most animals) towards baseline values at the 14 day time point, which reflects the
453 regeneration of the tissue.

454 T_2*-values are influenced by the presence of hemorrhage, calcification, iron, and depend on tissue
455 perfusion and oxygenation (2). We observed a significant decrease in T_2*-values during deformation
456 at day 0, which can be associated with reduced blood flow to the compressed TA muscle tissue (56).
457 In addition, removal of the top of the susceptibility matching alginate mold during compression of the
458 TA muscle at day 0, to allow access of the indentor, could have had influence on the T_2* values due to
459 increased field inhomogeneities. In part of the animals, areas with lower T_2*-values compared to
460 baseline were observed directly after load release at day 0, which can be an indication for the presence
461 of hemorrhage, most likely caused by disrupted muscle fibers. T_2* values at later time points (> day 5)
462 were also decreased, which can be explained by hemorrhages with the associated iron deposits and
463 phagocytic activity (50). The former peaked at day 3, although T_2* was not considerably different
464 from baseline at this time point. This can be explained by competing effects from edema, which
465 increases T_2* and hemorrhaging which lowers T_2*. At the final day 14 time point TA T_2* values were
466 still lower than baseline, which can be explained by the presence of fibrosis and remaining differences
467 in tissue cellularity as compared to control skeletal muscle (75).

468 The skeletal muscle water diffusivity depends on several tissue features, including tissue integrity,
469 cellularity, intracellular and extracellular water fractions, and the presence of edema (83). The mean
470 diffusivity MD, also referred to as apparent diffusion coefficient (ADC) has been previously
471 investigated in rat skeletal muscle under compression (76). The authors concluded that the skeletal
472 muscle water MD was stable under compression. A confounding factor in their experiments, however,
473 was the temperature changes in muscle tissue during the *in vivo* experiment, which probably obscured
474 the effects of compression on MD. We clearly observed a significant increase in MD during

deformation and in the first days after load release, which can be explained by the presence of edema and cell swelling (31, 47, 80, 111). The decrease in MD from > day 5 can be explained by restricted diffusion from newly formed small and dense packed myocytes (30). Our histopathological evaluation revealed mild to moderate presence of interstitial fibrosis, which will provide an additional decrease in MD by restricted water diffusion. However, the low correlation of MR parameters with fibrosis emphasizes that it is challenging to specifically detect fibrosis in skeletal muscle by MRI. The probable reason is that the MRI contrast is dominated by other pathological features, such as edema, inflammation, and hemorrhage.

Reduced flow in the main supplying blood vessel was observed in several animals by TOF MRA, which provides support to previous reports of extensive regions with low perfusion underneath and distal to the indentor (100). Furthermore, in some animals it appeared that surrounding vessels carried more blood to the deformed TA muscle, although this is difficult to quantify using TOF MRA. Previous measurements of increased perfusion in the lateral and posterior compartments support this observation (64). Similarly, the observed hyperemic response can be attributed to increased perfusion in the TA compartment after load release (41, 64, 100). A recommendation for future studies is the use of a quantitative MRI technique such as dynamic contrast enhanced, intravoxel incoherent motion, arterial spin labeling, or 4D flow.

Summarizing, the combination of multi-parametric MRI and histopathology provides the following principal observations, as indicted in Figure 11. T_2 and T_2-weighted MRI corresponded with edema, increased interstitial space, muscle cell damage, inflammatory onset, and inflammation. T_2* provided a readout of tissue perfusion, hemorrhages, and inflammation. MD is sensitive to the integrity of the tissue microstructure and reflects muscle degeneration and edema, as well as ECM remodeling during the muscle remodeling processes. TOF MRA provided information on occlusion of blood flow during the indentation period.

Although the recovery processes and remodeling after the damage-causing action were detailed in this study, there are also some limitations. As an example, the remodeling kinetics of damaged muscle was

variable between animals and may take up to 30 days (30, 110). Time to full remodeling depends on the extent of induced muscle damage, which was inevitably variable in this deep tissue injury rat model due to the inherent differences in the magnitude and angle of indentation, small anatomical variations between animals, the amount of induced ischemia by blockage of blood supply, and accumulation of waste products by differences in impaired lymphatic drainage (66). Furthermore, the damage development and the remodeling process hereafter may differ between muscles due to the difference in muscle geometry, muscle fiber distribution, and muscle fiber type. The extent and location of damage has previously been correlated to the values of deformation energy, which can be derived from FEA calculations (62). Additionally, it must be accepted that an animal model is a simplification of the human situation. As an example, thresholds for the damage-causing mechanisms, temporal profiles of recovery process and remodeling, are likely to differ between the two cases. Moreover, the in vivo changes in biochemical and bio-energetic processes as result of deformation, for example, pH decrease due to accumulation of waste products, were not determined. MR spectroscopy could provide such information (83, 101). On top of that, information on the physical performance of damaged skeletal muscle was lacking as no functional or performance-based data was collected (42).

The skeletal muscles of individuals at high risk of developing deep tissue injury and pressure ulcers in general, such as spinal-cord injury subjects, are likely to differ in structural composition when compared to those of ambulant subjects. Denervated muscle will become atrophic and fat infiltrated. This influences the mechanical properties of the muscle tissue and thus the way it deforms under compression. Moreover, differences in tissue perfusion and metabolism can influence the recovery and regeneration processes. It would therefore be important to study deep tissue injury in disease models, including models of muscle denervation, muscle atrophy, and fat-infiltrated muscle. In addition, the use of Magnetic Resonance Elastography (MRE) would provide a biomarker which reflects the viscoelastic behavior of muscle and the role of tissue stiffness on the development and remodeling of deep tissue injury (74).

To conclude, the present study provides several implications for understanding deep tissue injury etiology and for management of deep tissue injury in clinical practice. Importantly, we observed that

528 the initial tissue response to deformation occurred at some distance from the center of indentation,
529 affecting a relatively large area. First signs of damage development may therefore be detected away
530 from the deformed tissue, whereas current approaches for early detection generally focus on the actual
531 site of indentation. Secondly, a single damage causing event, involving 2 h of indentation, was
532 sufficient to cause extensive muscle damage that required at least 2 weeks to recover. Repetitive
533 loading of the tissue and longer loading periods are likely to exacerbate the extent of the damage.
534 Reloading of the damaged tissue should be avoided by appropriate measures in order to allow for
535 adequate remodeling. Finally, the multi-parametric MRI assessment provided specific imaging
536 parameters which may become diagnostic for deep tissue injury related muscle damage development
537 and remodeling. The quantitative changes over time for the various readouts (T_2, T_2*, and MD)
538 demonstrate that these combined parameters provide different and complementary information on the
539 extent, temporal evolution and microstructural basis of muscle damage.

Ethical approval

All animal experiments were approved by the local Animal Care and Use Committee (protocol 2013-047, Maastricht University, Maastricht, The Netherlands) and performed in accordance with the Directive 2010/63/EU for animal experiments of the European Union.

Acknowledgements

The authors thank Leonie Niesen, Jo Habets, David Veraart, Marije Janssen, Roy Lucassen, and Carlijn Tijsen - van Helvert for biotechnical assistance. Invaluable suggestions on statistics by dr. Koo Rijpkema (Department of Mathematics and Computer Science, Eindhoven University of Technology, The Netherlands) are gratefully acknowledged.

Grants

Dutch Technology Foundation STW, part of the Netherlands Organisation for Scientific Research (NWO) and the Ministry of Economic Affairs, Agriculture and Innovation (project number 12398). The European Cooperation in Science and Technology (COST) MYO-MRI action supported this research by funding a short term scientific mission (STSM) (project number BM1304-34240). The funders had no role in study design, data collection and analysis, decision to publish, or preparation of the manuscript.

Conflicts of interest

The authors state that they do not have a conflict of interest.

References

1. **Ababneh Z**, **Beloeil H**, **Berde CB**, **Gambarota G**, **Maier SE**, **Mulkern R V.** Biexponential parameterization of diffusion and T2 relaxation decay curves in a rat muscle edema model: Decay curve components and water compartments. *Magn Reson Med* 54: 524–531, 2005.

2. **Anderson L**. Cardiovascular T2-star (T2*) magnetic resonance for the early diagnosis of myocardial iron overload. *Eur Heart J* 22: 2171–2179, 2001.

3. **Ankrom MA**, **Bennett RG**, **Sprigle S**, **Langemo D**, **Black JM**, **Berlowitz DR**, **Lyder CH**. Pressure-Related Deep Tissue Injury under Intact Skin and the current pressure ulcer staging systems. *Adv Skin Wound Care* 18: 35–42, 2005.

4. **Aoi N**, **Yoshimura K**, **Kadono T**, **Nakagami G**, **Iizuka S**, **Higashino T**, **Araki J**, **Koshima I**, **Sanada H**. Ultrasound Assessment of Deep Tissue Injury in Pressure Ulcers: Possible Prediction of Pressure Ulcer Progression. *Plast Reconstr Surg* 124: 540–550, 2009.

5. **Bader DL**, **Barnhill RL**, **Ryan TJ**. Effect of externally applied skin surface forces on tissue vasculature. *Arch Phys Med Rehabil* 67: 807–811, 1986.

6. **Bader DL**, **Bouten CVC**, **Colin D**, **Oomens CWJJ**, **(Eds.)**. *Pressure Ulcer Research: Current and Future Perspectives*. Berlin: Springer Berlin Heidelberg, 2005.

7. **Beeckman D**, **Schoonhoven L**, **Fletcher J**, **Furtado K**, **Heyman H**, **Paquay L**, **De Bacquer D**, **Defloor T**. Pressure ulcers and incontinence-associated dermatitis: effectiveness of the Pressure Ulcer Classification education tool on classification by nurses. *Qual Saf Health Care* 19: e3, 2010.

8. **Bentzinger CF**, **Wang YX**, **Dumont NA**, **Rudnicki MA**. Cellular dynamics in the muscle satellite cell niche. *EMBO Rep* 14: 1062–1072, 2013.

9. **Black J**. National Pressure Ulcer Advisory Panel's updated pressure ulcer staging system. *Adv Skin Wound Care* 20: 269–274, 2007.

10. **Black JM**, **Brindle CT**, **Honaker JS**. Differential diagnosis of suspected deep tissue injury. *Int Wound J* 13: 531–539, 2016.

11. **Bosboom EM**, **Hesselink MK**, **Oomens CW**, **Bouten C V**, **Drost MR**, **Baaijens FP**. Passive transverse mechanical properties of skeletal muscle under in vivo compression. *J Biomech* 34: 1365–8, 2001.

12. **Bosboom EMH**, **Bouten CVC**, **Oomens CWJ**, **Baaijens FPT**, **Nicolay K**. Quantifying pressure sore-related muscle damage using high-resolution MRI. *J Appl Physiol* 95: 2235–40, 2003.

13. **Bosboom EMH**, **Bouten CVC**, **Oomens CWJ**, **Van Straaten HWM**, **Baaijens FPT**, **Kuipers H**. Quantification and localisation of damage in rat muscles after controlled loading - a new approach to study the aetiology of pressure sores. *Med Eng Phys* 23: 195–200, 2001.

14. **Bouten C V.**, **Oomens CWJ**, **Baaijens FP**, **Bader DL**. The etiology of pressure ulcers: skin deep or muscle bound? *Arch Phys Med Rehabil* 84: 616–9, 2003.

15. **Breuls RGM**, **Bouten CVC**, **Oomens CWJ**, **Bader DL**, **Baaijens FPT**. Compression Induced Cell Damage in Engineered Muscle Tissue: An In Vitro Model to Study Pressure Ulcer Aetiology. *Ann Biomed Eng* 31: 1357–1364, 2003.

16. **Bryant ND**, **Li K**, **Does MD**, **Barnes S**, **Gochberg DF**, **Yankeelov TE**, **Park JH**, **Damon BM**. Multi-parametric MRI characterization of inflammation in murine skeletal muscle. *NMR Biomed* 27:

716–25, 2014.

17. **Byrne DW**, **Salzberg CA**. Major risk factors for pressure ulcers in the spinal cord disabled: a literature review. *Spinal Cord* 34: 255–263, 1996.

18. **Carlier PG**, **Marty B**, **Scheidegger O**, **Loureiro de Sousa P**, **Baudin P-Y**, **Snezhko E**, **Vlodavets D**. Skeletal Muscle Quantitative Nuclear Magnetic Resonance Imaging and Spectroscopy as an Outcome Measure for Clinical Trials. *J Neuromuscul Dis* 3: 1–28, 2016.

19. **Ceelen KK**, **Stekelenburg A**, **Loerakker S**, **Strijkers GJ**, **Bader DL**, **Nicolay K**, **Baaijens FPT**, **Oomens CWJ**. Compression-induced damage and internal tissue strains are related. *J Biomech* 41: 3399–3404, 2008.

20. **Coleman S**, **Nixon J**, **Keen J**, **Wilson L**, **McGinnis E**, **Dealey C**, **Farrin A**, **Dowding D**, **Schols JMGAGA**, **Cuddigan J**, **Berlowitz D**, **Vowden P**, **Schoonhoven L**, **Bader DL**, **Gefen A**, **Oomens CWJJ**, **Nelson EA**, **Stubbs N**, **Farrin A**, **Dowding D**, **Schols JMGAGA**, **Cuddigan J**, **Berlowitz D**, **Jude E**, **Vowden P**, **Schoonhoven L**, **Bader DL**, **Gefen A**, **Oomens CWJJ**, **Nelson EA**. A new pressure ulcer conceptual framework. *J Adv Nurs* 70: 2222–2234, 2014.

21. **Cornelissen LH**, **Bronneberg D**, **Bader DL**, **Baaijens FPT**, **Oomens CWJ**. The transport profile of cytokines in epidermal equivalents subjected to mechanical loading. *Ann Biomed Eng* 37: 1007–1018, 2009.

22. **Cutlip RG**, **Baker BA**, **Hollander M**, **Ensey J**. Injury and adaptive mechanisms in skeletal muscle. *J Electromyogr Kinesiol* 19: 358–372, 2009.

23. **Cutlip RG**, **Hollander MS**, **Johnson GA**, **Johnson BW**, **Friend SA**, **Baker BA**. Magnetic resonance imaging of graded skeletal muscle injury in live rats. *Environ Health Insights* 8: 31–9, 2014.

24. **Damon BM**. MRI in Pre-Clinical Models of Muscle Disease. *Proc Intl Soc Mag Reson Med* 19, 2011.

25. **Dealey C**, **Lindholm C**. Pressure Ulcer Classification. In: *Science and Practice of Pressure Ulcer Management*, edited by Romanelli M., Clark M., Colin D. & Defloor T. E. London: European Pressure Ulcer Advisory Panel & Springler-Verlag, 2006, p. 38–41.

26. **Dealey C**, **Posnett J**, **Walker A**. The cost of pressure ulcers in the United Kingdom. *J Wound Care* 21: 261–266, 2012.

27. **Defloor T**, **Schoonhoven L**, **Katrien V**, **Weststrate J**, **Myny D**. Reliability of the European pressure ulcer advisory panel classification system. *J Adv Nurs* 54: 189–198, 2006.

28. **Dinsdale SM**. Decubitus ulcers: role of pressure and friction in causation. *Arch Phys Med Rehabil* 55: 147–52, 1974.

29. **Edsberg LE**, **Black JM**, **Goldberg M**, **McNichol L**, **Moore L**, **Sieggreen M**. Revised National Pressure Ulcer Advisory Panel Pressure Injury Staging System: Revised Pressure Injury Staging System. *J wound, ostomy, Cont Nurs Off Publ Wound, Ostomy Cont Nurses Soc* 43: 585–597, 2016.

30. **Esposito A**, **Campana L**, **Palmisano A**, **De Cobelli F**, **Canu T**, **Santarella F**, **Colantoni C**, **Monno A**, **Vezzoli M**, **Pezzetti G**, **Manfredi AA**, **Rovere-Querini P**, **De Maschio A**, **Maschio A Del**, **De Maschio A**. Magnetic Resonance Imaging at 7T Reveals Common Events in Age-Related Sarcopenia and in the Homeostatic Response to Muscle Sterile Injury. *PLoS One* 8: 1–9, 2013.

31. **Fan RH**, **Does MD**. Compartmental relaxation and diffusion tensor imaging measurements *in vivo* in λ-carrageenan-induced edema in rat skeletal muscle. *NMR Biomed* 21: 566–573, 2008.

32. **Feng S**, **Chen D**, **Kushmerick M**, **Lee D**. Multiparameter MRI analysis of the time course of induced muscle damage and regeneration. *J Magn Reson Imaging* 40: 779–788, 2014.

33. **Fleck CA**. Deep Tissue Injury: What, Why and When? *Wound Care Canada* 5: 10–13, 2007.

34. **Fleck CA**. Suspected Deep Tissue Injury. *Adv Skin Wound Care* 20: 413–415, 2007.

35. **Forbes SC**, **Willcocks RJ**, **Rooney WD**, **Walter GA**, **Vandenborne K**. MRI quantifies neuromuscular disease progression. *Lancet Neurol* 15: 26–28, 2016.

36. **Froeling M**. DTITools. *Zenodo* (2016). doi: 10.5281/zenodo.54685.

37. **Gawlitta D**, **Oomens CWJ**, **Bader DL**, **Baaijens FPT**, **Bouten CVC**. Temporal differences in the influence of ischemic factors and deformation on the metabolism of engineered skeletal muscle. *J Appl Physiol* 103: 464–473, 2007.

38. **Gefen A**, **Farid KJ**, **Shaywitz I**. A review of deep tissue injury development, detection, and prevention: shear savvy. *Ostomy Wound Manage* 59: 26–35, 2013.

39. **Gefen A**, **van Nierop B**, **Bader DL**, **Oomens CW**. Strain-time cell-death threshold for skeletal muscle in a tissue-engineered model system for deep tissue injury. *J Biomech* 41: 2003–2012, 2008.

40. **Goldstein B**, **Sanders J**. Skin response to repetitive mechanical stress: A new experimental model in pig. *Arch Phys Med Rehabil* 79: 265–272, 1998.

41. **Gondin J**, **Vilmen C**, **Cozzone PJ**, **Bendahan D**, **Duhamel G**. High-field (11.75T) multimodal MR imaging of exercising hindlimb mouse muscles using a non-invasive combined stimulation and force measurement device. *NMR Biomed* 27: 870–879, 2014.

42. **Guralnik JM**, **Simonsick EM**, **Ferrucci L**, **Glynn RJ**, **Berkman LF**, **Blazer DG**, **Scherr PA**, **Wallace RB**. A Short Physical Performance Battery Assessing Lower Extremity Function: Association With Self-Reported Disability and Prediction of Mortality and Nursing Home Admission. *J Gerontol* 49: M85–M94, 1994.

43. **Guttmann L**. The problem of treatment of pressure sores in spinal paraplegics. *Br J Plast Surg* 8: 196–213, 1955.

44. **Häggström M**. Medical gallery of Mikael Häggström 2014. *WikiJournal Med* 1, 2014.

45. **Hagisawa S**, **Ferguson-Pell MW**, **Palmieri VR**, **Cochran G V**. Pressure sores: a biochemical test for early detection of tissue damage. *Arch Phys Med Rehabil* 69: 668–71, 1988.

46. **Hammers DW**, **Merritt EK**, **Matheny W**, **Adamo ML**, **Walters TJ**, **Estep JS**, **Farrar RP**. Functional deficits and insulin-like growth factor-I gene expression following tourniquet-induced injury of skeletal muscle in young and old rats. *J Appl Physiol* 105: 1274–1281, 2008.

47. **Heemskerk AM**, **Strijkers GJ**, **Drost MR**, **van Bochove GS**, **Nicolay K**. Skeletal Muscle Degeneration and Regeneration after Femoral Artery Ligation in Mice: Monitoring with Diffusion MR Imaging. *Radiology* 243: 413–421, 2007.

48. **Hollingsworth KG**, **de Sousa PL**, **Straub V**, **Carlier PG**. Towards harmonization of protocols for MRI outcome measures in skeletal muscle studies: Consensus recommendations from two TREAT-NMD NMR workshops, 2 May 2010, Stockholm, Sweden, 1–2 October 2009, Paris, France. *Neuromuscul Disord* 22: S54–S67, 2012.

49. **Houwing R**, **Overgoor M**, **Kon M**, **Jansen G**, **van Asbeck BS**, **Haalboom JRE**. Pressure-induced skin lesions in pigs: reperfusion injury and the effects of vitamin E. *J Wound Care* 9: 36–40, 2000.

50. **Huelnhagen T**, **Paul K**, **Ku M-C**, **Serradas Duarte T**, **Niendorf T**. Myocardial T2* Mapping with Ultrahigh Field Magnetic Resonance: Physics and Frontier Applications. *Front Phys* 5, 2017.

51. **Jahnigen DW**, **Baxter CR**, **Bodenbender RH**. Pressure ulcers: prevalence, cost and risk assessment: Consensus development conference statement. *Decubitus* 2: 24–30, 1989.

52. **Järvinen TAH**, **Järvinen TLN**, **Kääriäinen M**, **Kalimo H**, **Järvinen M**. Muscle Injuries. *Am J Sports Med* 33: 745–764, 2005.

53. **Kan HE**, **Scheenen TWJ**, **Wohlgemuth M**, **Klomp DWJ**, **van Loosbroek-Wagenmans I**, **Padberg GW**, **Heerschap A**. Quantitative MR imaging of individual muscle involvement in facioscapulohumeral muscular dystrophy. *Neuromuscul Disord* 19: 357–362, 2009.

54. **Knight SL**, **Taylor RP**, **Polliack AA**, **Bader DL**. Establishing predictive indicators for the status of loaded soft tissues. *J Appl Physiol* 90: 2231–7, 2001.

55. **Kosiak M**. Etiology of decubitus ulcers. *Arch Phys Med Rehabil* 42: 19, 1961.

56. **Lebon V**, **Brillault-Salvat C**, **Bloch G**, **Leroy-Willig A**, **Carlier PG**. Evidence of muscle BOLD effect revealed by simultaneous interleaved gradient-echo NMRI and myoglobin NMRS during leg ischemia. *Magn Reson Med* 40: 551–558, 1998.

57. **Li K**, **Dortch RD**, **Welch EB**, **Bryant ND**, **Buck AKW**, **Towse TF**, **Gochberg DF**, **Does MD**, **Damon BM**, **Park JH**. Multi-parametric MRI characterization of healthy human thigh muscles at 3.0 T - relaxation, magnetization transfer, fat/water, and diffusion tensor imaging. *NMR Biomed* 27: 1070–1084, 2014.

58. **Linder-Ganz E**, **Engelberg S**, **Scheinowitz M**, **Gefen A**. Pressure-time cell death threshold for albino rat skeletal muscles as related to pressure sore biomechanics. *J Biomech* 39: 2725–32, 2006.

59. **Linder-Ganz E**, **Gefen A**. Mechanical compression-induced pressure sores in rat hindlimb: muscle stiffness, histology, and computational models. *J Appl Physiol* 96: 2034–49, 2004.

60. **Linder-Ganz E**, **Gefen A**. The effects of pressure and shear on capillary closure in the microstructure of skeletal muscles. *Ann Biomed Eng* 35: 2095–107, 2007.

61. **Loerakker S**. The relative contributions of muscle deformation and ischaemia to pressure ulcer development. first. Eindhoven: Universiteitsdrukkerij TU Eindhoven, Eindhoven, The Netherlands, 2011.

62. **Loerakker S**, **Bader DL**, **Baaijens FPT**, **Oomens CWJ**. Which factors influence the ability of a computational model to predict the in vivo deformation behaviour of skeletal muscle? *Comput Methods Biomech Biomed Engin* 16: 338–45, 2013.

63. **Loerakker S**, **Huisman ES**, **Seelen HAM**, **Glatz JFC**, **Baaijens FPT**, **Oomens CWJ**, **Bader DL**. Plasma variations of biomarkers for muscle damage in male nondisabled and spinal cord injured subjects. *J Rehabil Res Dev* 49: 361–72, 2012.

64. **Loerakker S**, **Manders E**, **Strijkers GJ**, **Nicolay K**, **Baaijens FPT**, **Bader DL**, **Oomens CWJ**. The effects of deformation, ischemia, and reperfusion on the development of muscle damage during prolonged loading. *J Appl Physiol* 111: 1168–1177, 2011.

65. **Loerakker S**, **Oomens CWJ**, **Manders E**, **Schakel T**, **Bader DL**, **Baaijens FPT**, **Nicolay K**, **Strijkers GJ**. Ischemia-reperfusion injury in rat skeletal muscle assessed with T2-weighted and dynamic contrast-enhanced MRI. *Magn Reson Med* 66: 528–537, 2011.

66. **Loerakker S**, **Stekelenburg A**, **Strijkers GJ**, **Rijpkema JJM**, **Baaijens FPT**, **Bader DL**, **Nicolay K**, **Oomens CWJ**. Temporal Effects of Mechanical Loading on Deformation-Induced Damage in

Skeletal Muscle Tissue. *Ann Biomed Eng* 38: 2577–2587, 2010.

67. **Lovering RM**, **Mcmillan AB**, **Gullapalli RP**. Location of myofiber damage in skeletal muscle after lengthening contractions. *Muscle and Nerve* 40: 589–594, 2009.

68. **Makhsous M**, **Lin F**, **Pandya A**, **Pandya MS**, **Chadwick CC**. Elevation in the Serum and Urine Concentration of Injury-Related Molecules After the Formation of Deep Tissue Injury in a Rat Spinal Cord Injury Pressure Ulcer Model. *PM&R* 2: 1063–1065, 2010.

69. **Mann CJ**, **Perdiguero E**, **Kharraz Y**, **Aguilar S**, **Pessina P**, **Serrano AL**, **Muñoz-Cánoves P**. Aberrant repair and fibrosis development in skeletal muscle. *Skelet Muscle* 1: 21, 2011.

70. **May D a**, **Disler DG**, **Jones E a**, **Balkissoon A a**, **Manaster BJ**. Abnormal Signal Intensity in Skeletal Muscle at MR Imaging: Patterns, Pearls, and Pitfalls. *RadioGraphics* 20: S295–S315, 2000.

71. **Miller GE**, **Seale J**. Lymphatic clearance during compressive loading. *Lymphology* 14: 161–166, 1981.

72. **Morrow JM**, **Sinclair CDJ**, **Fischmann A**, **Machado PM**, **Reilly MM**, **Yousry TA**, **Thornton JS**, **Hanna MG**. MRI biomarker assessment of neuromuscular disease progression: a prospective observational cohort study. *Lancet Neurol* 15: 65–77, 2016.

73. **Nagel T**, **Loerakker S**, **Oomens CW**. A theoretical model to study the effects of cellular stiffening on the damage evolution in deep tissue injury. *Comput Methods Biomech Biomed Engin* 12: 585–597, 2009.

74. **Nelissen JL**, **de Graaf L**, **Traa WA**, **Schreurs TJL**, **Moerman KM**, **Nederveen AJ**, **Sinkus R**, **Oomens CWJ**, **Nicolay K**, **Strijkers GJ**. A MRI-Compatible Combined Mechanical Loading and MR Elastography Setup to Study Deformation-Induced Skeletal Muscle Damage in Rats. *PLoS One* 12: e0169864, 2017.

75. **van Nierop BJ**, **Bax NAM**, **Nelissen JL**, **Arslan F**, **Motaal AG**, **de Graaf L**, **Zwanenburg JJJMM**, **Luijten PR**, **Nicolay K**, **Strijkers GJ**. Assessment of Myocardial Fibrosis in Mice Using a T2*-Weighted 3D Radial Magnetic Resonance Imaging Sequence. *PLoS One* 10: e0129899, 2015.

76. **van Nierop BJ**, **Stekelenburg A**, **Loerakker S**, **Oomens CW**, **Bader DL**, **Strijkers GJ**, **Nicolay K**. Diffusion of water in skeletal muscle tissue is not influenced by compression in a rat model of deep tissue injury. *J Biomech* 43: 570–5, 2010.

77. **NPUAP/EPUAP/PPPIA**, **National Pressure Ulcer Advisory Panel, European Pressure Ulcer Advisory Panel and Pan Pacific Pressure Injury Alliance**. *Prevention and treatment of pressure ulcers: clinical practice guideline*. Perth, Australia, Western Australia: Cambridge Media, 2014.

78. **Oomens CWJ**, **Bader DL**, **Loerakker S**, **Baaijens FP**. Pressure Induced Deep Tissue Injury Explained. *Ann Biomed Eng* 43: 297–305, 2015.

79. **Oomens CWJ**, **Loerakker S**, **Bader DL**. The importance of internal strain as opposed to interface pressure in the prevention of pressure related deep tissue injury. *J Tissue Viability* 19: 35–42, 2010.

80. **Oudeman J**, **Nederveen AJ**, **Strijkers GJ**, **Maas M**, **Luijten PR**, **Froeling M**. Techniques and applications of skeletal muscle diffusion tensor imaging: A review. *J Magn Reson Imaging* 43: 773–788, 2016.

81. **Park J**, **Wicki J**, **Knoblaugh SE**, **Chamberlain JS**, **Lee D**. Multi-Parametric MRI at 14T for Muscular Dystrophy Mice Treated with AAV Vector-Mediated Gene Therapy. *PLoS One* 10: e0124914, 2015.

82. **Peirce SM**, **Skalak TC**, **Rodeheaver GT**. Ischemia-reperfusion injury in chronic pressure ulcer formation: A skin model in the rat. *Wound Repair Regen* 8: 68–76, 2000.

83. **Prompers JJ**, **Jeneson JAL**, **Drost MR**, **Oomens CCW**, **Strijkers GJ**, **Nicolay K**. Dynamic MRS and MRI of skeletal muscle function and biomechanics. *NMR Biomed* 19: 927–953, 2006.

84. **Quintavalle P**. Use of High-resolution, High-frequency diagnostic ultrasound to investigate the pathogenesis of pressure ulcer development. *Adv. Skin Wound Care*. .

85. **Reddy NPN**, **Cochran GGVB**, **Krouskop TAT**. Interstitial fluid flow as a factor in decubitus ulcer formation. *J Biomech* 14: 879–881, 1981.

86. **Redelings MD**, **Lee NE**, **Sorvillo F**. Pressure ulcers: more lethal than we thought? *Adv Skin Wound Care* 18: 367–72, 2005.

87. **Reynolds TM**, **Stokes A**, **Russell L**. Assessment of a prognostic biochemical indicator of nutrition and inflammation for identification of pressure ulcer risk. *Br J Nurs* 7: 888–90, 2006.

88. **Richbourg L**, **Smith J**, **Dunzweiler S**. Suspected Deep Tissue Injury Evaluated by North Carolina WOC Nurses. *J Wound, Ostomy Cont Nurs* 38: 655–660, 2011.

89. **Rodriguez GP**, **Claus-Walker J**. Biochemical changes in skin composition in spinal cord injury: a possible contribution to decubitus ulcers. *Paraplegia* 26: 302–9, 1988.

90. **Salameh N**. Early Detection of Steatohepatitis in Fatty Rat Liver by Using MR Elastography. *J Appl Physiol* (2006). doi: 10.1152/japplphysiol.01115.2006.-A.

91. **Salcido R**. Heel Pressure Ulcers: Purple Heel and Deep Tissue Injury. *Adv Skin Wound Care* 24: 374–380, 2012.

92. **Salcido R**. Uncritical transfer of terminology to establish causation: deep tissue injury. *Adv Ski Wound Care* 27: 104, 2014.

93. **Schoonhoven L**, **Defloor T**, **Van Der Tweel I**, **Buskens E**, **Grypdonck MHF**. Risk indicators for pressure ulcers during surgery. *Appl Nurs Res* 15: 163–173, 2002.

94. **Severens**. The cost of illness of pressure ulcers in the Netherlands. *Adv Ski wound care* 15: 72–77, 2002.

95. **Shea JD**. Pressure Sores Classification and Management. *Clin Orthop Relat Res* 112: 89–100, 1975.

96. **Siu PM**, **Tam EW**, **Teng BT**, **Pei XM**, **Ng JW**, **Benzie IF**, **Mak AF**. Muscle apoptosis is induced in pressure-induced deep tissue injury. *J Appl Physiol* 107: 1266–1275, 2009.

97. **Stekelenburg A**. Compression-induced deep tissue injury examined with magnetic resonance imaging and histology. *J Appl Physiol* 100: 1946–1954, 2006.

98. **Stekelenburg A**, **Gawlitta D**, **Bader DL**, **Oomens CW**. Deep tissue injury: how deep is our understanding? *Arch Phys Med Rehabil* 89: 1410–1413, 2008.

99. **Stekelenburg A**, **Oomens CWJ**, **Strijkers GJ**, **de Graaf L**, **Bader DL**, **Nicolay K**. A new MR-compatible loading device to study in vivo muscle damage development in rats due to compressive loading. *Med Eng Phys* 28: 331–338, 2006.

100. **Stekelenburg A**, **Strijkers GJ**, **Parusel H**, **Bader DL**, **Nicolay K**, **Oomens CW**. Role of ischemia and deformation in the onset of compression-induced deep tissue injury: MRI-based studies in a rat model. *J Appl Physiol* 102: 2002–11, 2007.

101. **Strijkers GJ**, **Prompers JJ**, **Nicolay K**. Magnetic Resonance Imaging and Spectrocopy of Pressure Ulcers. *Press. Ulcer Res. Curr. Futur. Perspect.* (2005). doi: 10.1007/3-540-28804-X.

102. **Taylor RP**, **Polliack AA**, **Bader DL**. The analysis of metabolites in human sweat: Analytical methods and potential application to investigation of pressure ischaemia of soft tissues. *Ann Clin Biochem* 31: 18–24, 1994.

103. **Tsuji S**, **Ichioka S**, **Sekiya N**, **Nakatsuka T**. Analysis of ischemia-reperfusion injury in a microcirculatory model of pressure ulcers. *Wound Repair Regen* 13: 209–215, 2005.

104. **Ünal S**, **Özmen S**, **DemIr Y**, **Yavuzer R**, **LatIfoglu O**, **Atabay K**. The effect of gradually increased blood flow on ischemia-reperfusion injury. *Ann Plast Surg* 47: 412–416, 2001.

105. **VanGilder C**, **MacFarlane GD**, **Harrison P**, **Lachenbruch C**, **Meyer S**. The Demographics of Suspected Deep Tissue Injury in the United States. *Adv Skin Wound Care* 23: 254–261, 2010.

106. **Winkler T**, **Von Roth P**, **Matziolis G**, **Schumann MR**, **Hahn S**, **Strube P**, **Stoltenburg-Didinger G**, **Perka C**, **Duda GN**, **Tohtz S V.** Time course of skeletal muscle regeneration after severe trauma: Muscle function against the background of MRI and histological findings. *Acta Orthop* 82: 102–111, 2011.

107. **Yabunaka K**, **Iizaka S**, **Nakagami G**, **Fujioka M**, **Sanada H**. Three-dimensional ultrasound imaging of the pressure ulcer. A case report. *Med Ultrason* 17: 404, 2015.

108. **Yushkevich PA**, **Piven J**, **Hazlett HC**, **Smith RG**, **Ho S**, **Gee JC**, **Gerig G**. User-guided 3D active contour segmentation of anatomical structures: Significantly improved efficiency and reliability. *Neuroimage* 31: 1116–1128, 2006.

109. **Zaccagnini G**, **Palmisano A**, **Canu T**, **Maimone B**, **Russo FM Lo**, **Ambrogi F**, **Gaetano C**, **De Cobelli F**, **Del Maschio A**, **Esposito A**. Magnetic resonance imaging allows the evaluation of tissue damage and regeneration in a mouse model of critical limb ischemia. *PLoS One* 10: e0142111, 2015.

110. **Zaccagnini G**, **Palmisano A**, **Canu T**, **Maimone B**, **Russo FM Lo**, **Ambrogi F**, **Gaetano C**, **De Cobelli F**, **Del Maschio A**, **Esposito A**, **Lo Russo FM**, **Ambrogi F**, **Gaetano C**, **De Cobelli F**, **Del Maschio A**, **Esposito A**, **Martelli F**. Magnetic resonance imaging allows the evaluation of tissue damage and regeneration in a mouse model of critical limb ischemia. *PLoS One* 10: e0142111, 2015.

111. **Zaraiskaya T**, **Kumbhare D**, **Noseworthy MD**. Diffusion tensor imaging in evaluation of human skeletal muscle injury. *J Magn Reson Imaging* 24: 402–408, 2006.

Table captions

Table 1. Experimental groups.

Measured time points, number of animals, number of selected animals for histology, and the MRI protocol are indicated per group. [#]All animals were sacrificed after the last time point, followed by excision and storage of the control and deformed TA muscle for histology. [##]In some animals part of the MRI protocol was omitted due to unforeseen experimental problems.

Table 2. Quantitative MRI parameter values.

Quantitative MRI parameter values of the TA muscle (mean ± sd) of all for statistical analysis selected animals pre, during, and at various time points post indentation. The number of animals is indicated for each parameter. The asterisk (*) indicates a significant difference (*** for $p<0.001$, ** for $p<0.01$, * for $p<0.05$) versus baseline value at day 0 pre.

Table 3. Pathological evaluation of H&E and TRI stained control and deformed TA muscle.

Scoring for degeneration: 1 = 0-5%, 2 = 5-20%, 3 = 20-40%, 4 = >40% of slide area; severity of degeneration indicated by min (minimal), mld (mild), mod (moderate) and sev (severe). For necrosis, edema, hemorrhage, fibrosis, neutrophils, macrophages, and lymphocytes/plasma cells scoring is: 0 = normal, 1 = minimal, 2 = mild, 3 = moderate and 4 = severe. The number of animals scored at each time point is indicated. Values are mean ± standard deviation. The asterisk (*) indicates a significant difference (*** for $p<0.001$, ** for $p<0.01$, * for $p<0.05$) versus control TA muscle.

Table 4. Correlation of quantitative MRI parameters and pathological evaluation

Spearman correlation coefficient ρ. Spearman correlation coefficient ρ was tested for significance. The number of animals is indicated for each parameter. The asterisk (*) indicates a significant correlation (*** for $p<0.001$, ** for $p<0.01$, * for $p<0.05$).

Figure captions

Figure 1. T_2-weighted MR images of the TA muscle of a representative rat pre, during, and post 2 h deformation, central as well as proximal and distal to the indentor. In the central slice the indentor, which compressed the TA muscle towards the tibia bone, is visible. A large portion of the TA revealed high intensity after compression in the central slice but also in the distal and proximal slices. The EDL muscle displayed high intensity distally during indentation.

Figure 2. T_2-weighted MR images pre, during and post 2 h deformation of the TA muscle. Central slice position at position of indentor shows the deformation of the TA muscle towards the tibia bone together with distal and proximal located slices. High intensity signal in TA muscle tissue was observed during deformation distally to the center of deformation. Post deformation no high intensity signal was observed in the TA compartment.

Figure 3. Axial and coronal T_2-maps pre, during (multiple time points) and post indentation of the TA muscle. The numbers in the coronal images highlight regions in EDL and TA with elevated T_2 values during and after indentation. Legend for the color scaling of the T_2 (0-150 ms) is shown on the right.

Figure 4. Axial and coronal T_2- and T_2*-maps pre and post deformation at day 0. A region with reduced T_2 and T_2* values is indicated by the solid arrows. Legends for the color scaling of the T_2 (0-150 ms) and T2* (0-60 ms) are shown at the bottom.

Figure 5. Longitudinal multi-parametric MRI of one representative rat. From top to bottom: axial T_2-weighted (T_2w), T_2, T_2*, and MD maps, and coronal MIPs of the TOF angiography. Legends for the color scaling of the T_2 (0-150 ms), T_2* (0-60 ms), and MD (0.5-2x10^{-3} mm^2/s) maps are shown on the right.

Figure 6. Angiogram MIPs over time of RAT-005 and RAT-007. During deformation the indenter (orange arrows) applying load to the TA muscle is visible. The saphenous artery is centrally located. Reduced flow in the saphenous artery in RAT-007 is indicated with blue arrow. Hyperemic response is indicated with green arrow. Individual time-courses of the mean parametric values of RAT-005 and RAT-007 are also shown in Figure 8.

Figure 7. TA muscle T_2, T_2*, and MD-values of all animals during the time course of the whole experiment. The 2 h deformation period is indicated with the gray area. Each open circle is a quantitative MRI measurement of a single animal at given time. The thick solid lines are the mean parameter values of all animals at the different time periods pre, during, and post indentation. Not all measurements were performed at exactly the same time or repeated several times in close succession. Therefore, mean values were calculated per time period, defined as: pre = -120-0 min, during indentation = 0-120 min, post = 120-300 min, as well as at 3, 5, 7, 10, and 14 days post indentation. Two distinctly different animals are highlighted by the green and magenta colored data points.

Representative quantitative maps of both highlighted animals are displayed as inset. Quantitative parameter maps of these two animals at all time points are presented in Figure 8.

Figure 8. Mean T_2, T_2*, and MD values in the TA of individual animals of group VI over time. T_2, T_2*, and MD in A, B and C, respectively. Each line represents a single animal, points on the line indicate the measurement timepoints. Legend is depicted in subfigure A. The 2 h deformation period is indicated with a gray bar. RAT-001 and RAT-002 were also selected in Figure 6 and Figure 8.

Figure 9. Multi-parametric MRI readouts of the two selected animals of Figure 6, with animal identification number RAT-001 and RAT-002. The two animals were selected as two extremes to exemplify the spread in measured MRI readouts and response to 2 h of deformation in the group of animals. In comparison to RAT-002, RAT-001 showed altered MRI readouts (e.g. decreased MD and T_2*, low intensity T_2-weighted (T_2w) region at day 14) up to 14 days after damage inducing deformation. For RAT-002 only a minor response, of collateral blood vessels, on the angiogram during deformation was observed. All other MRI readouts of RAT-002 appeared normal.

Figure 10. Representative H&E and TRI histological sections next to the various multi-parametric MRI readouts at day 0, 3, 5, and 14. For day 14 one animal with mild (RAT-005) and one with severe (RAT-006) damage is shown. Individual time-courses of the mean parametric values of RAT-005 and RAT-006 were also shown in Figure 8. Legends for the color scaling of the T_2 (0-150 ms), T_2* (0-60 ms), and MD (0.5-2x10^{-3} mm^2/s) maps are shown on the bottom.

Figure 11. Time-course of tissue damage and remodeling in the rat model of deep tissue injury characterized by multi-parametric MRI (T_2, T_2*, MD, and MRA) and linked to histopathology. The neutrophil, lymphocyte, and erythrocyte cell types were designed by Mikael Häggström, used with permission (44).

Supplemental information captions

Supplemental Content 1. Movie of rotating TOF angiogram MIPs over time of RAT-005 and RAT-007, also shown in Figure 6. During deformation the indenter applying load to the TA muscle is visible. The saphenous artery is centrally located. RAT-007 showed reduced flow in the saphenous artery followed by a hyperemic response.

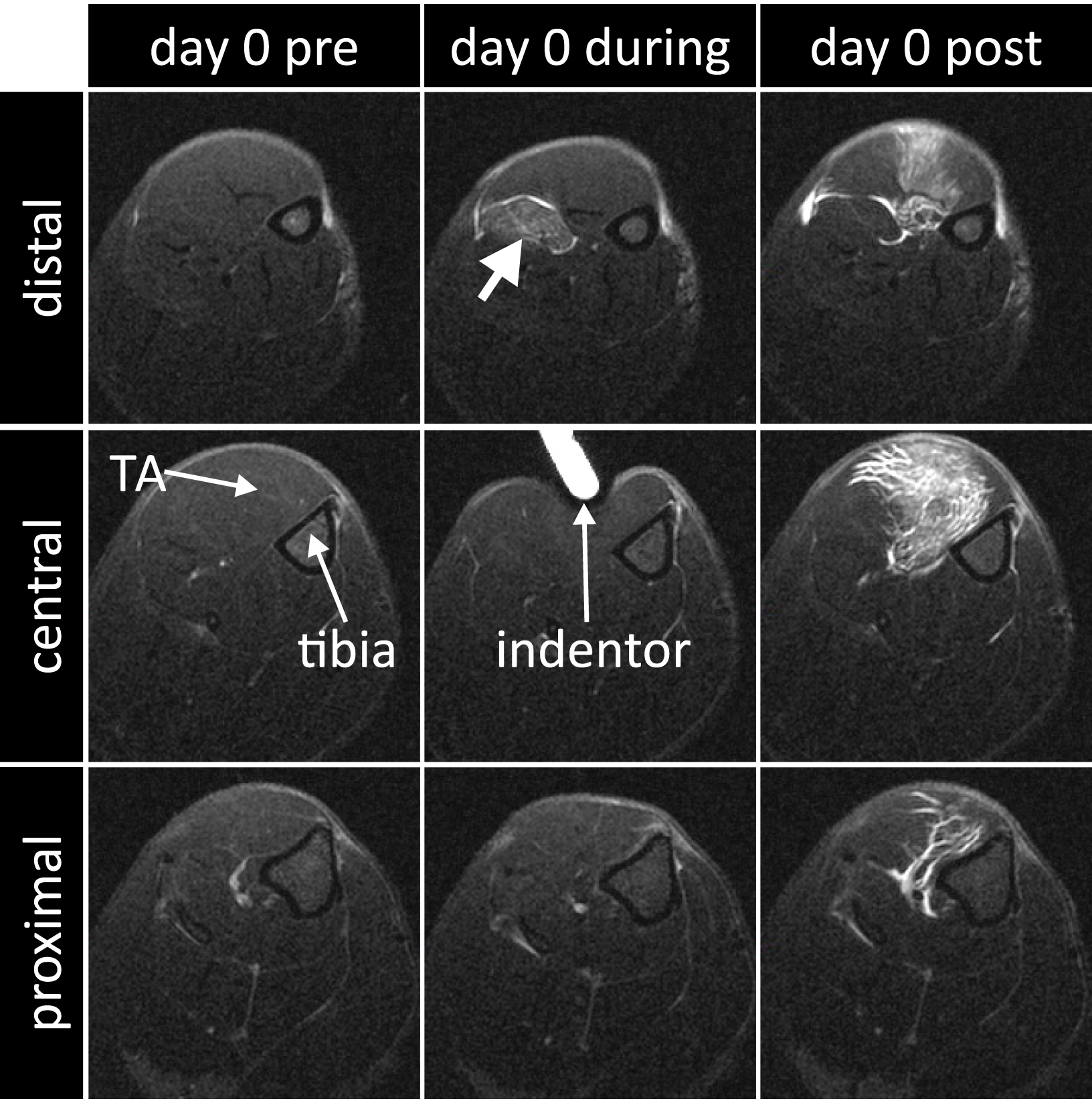
day 0 pre
day 0 during
day 0 post
distal
central
proximal
TA
tibia
indentor

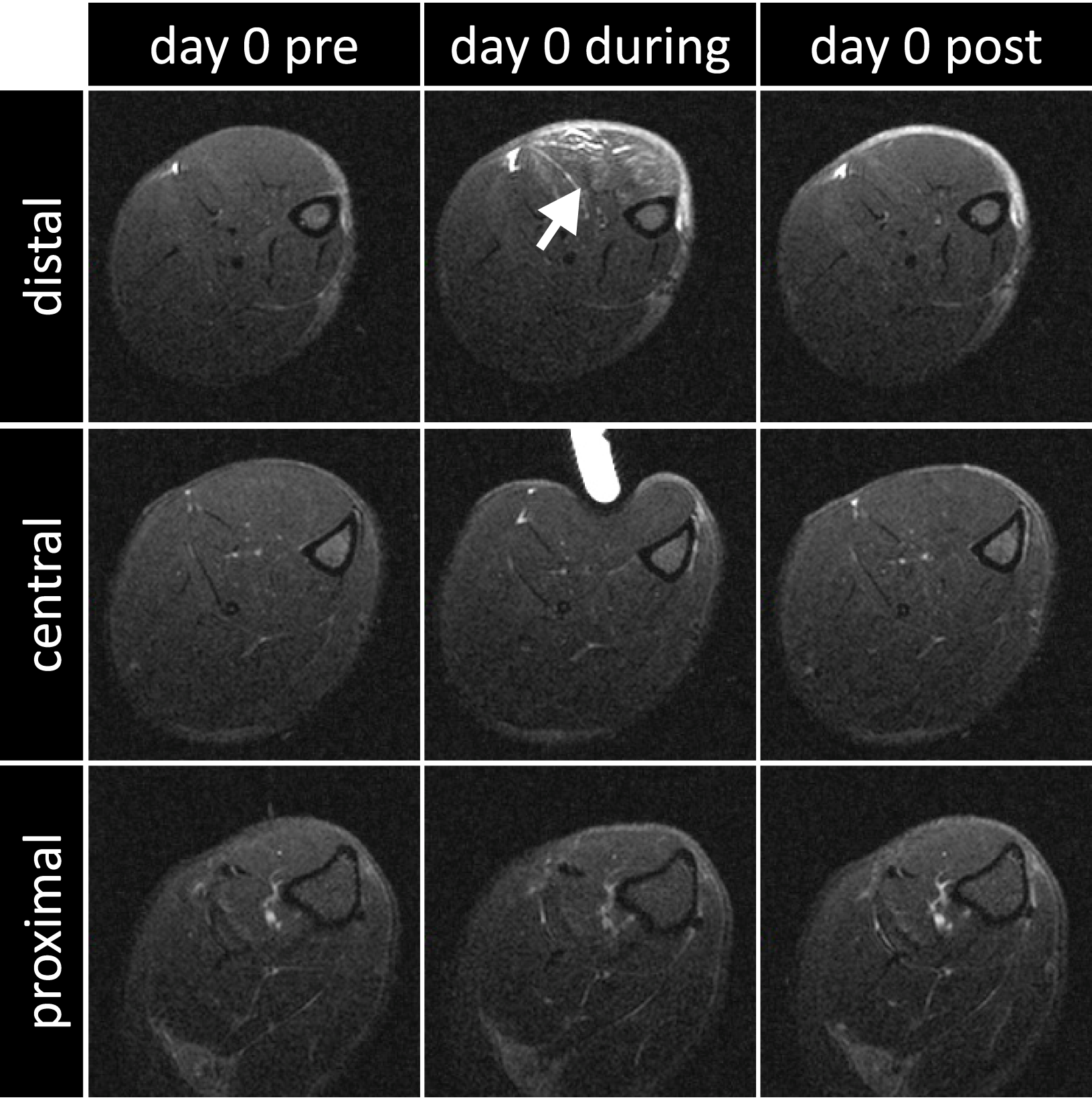
day 0 pre
day 0 during
day 0 post
distal
central
proximal

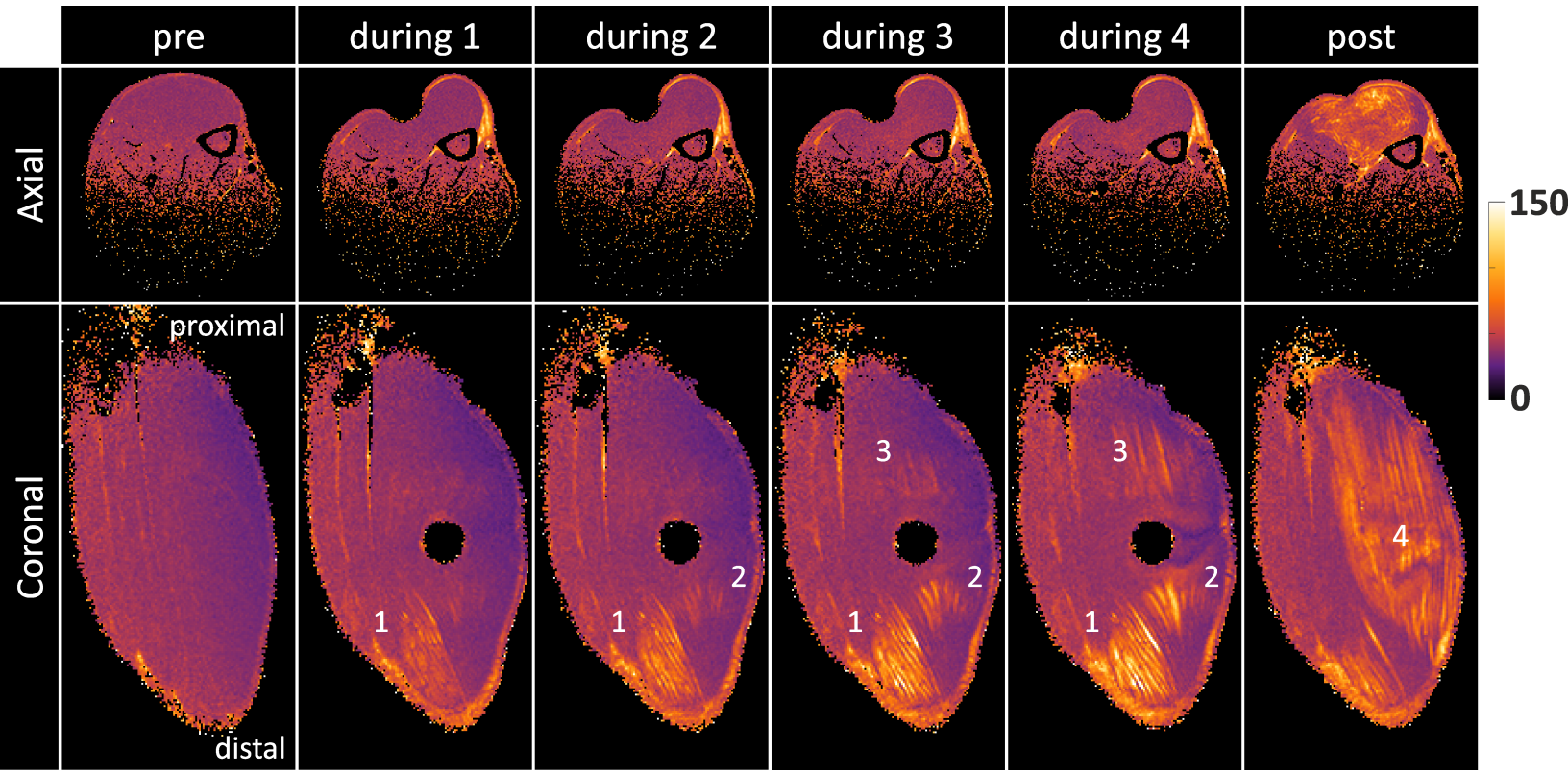
pre
during 1
during 2
during 3
during 4
post
Axial
Coronal
proximal
distal
1
2
3
4
150
0

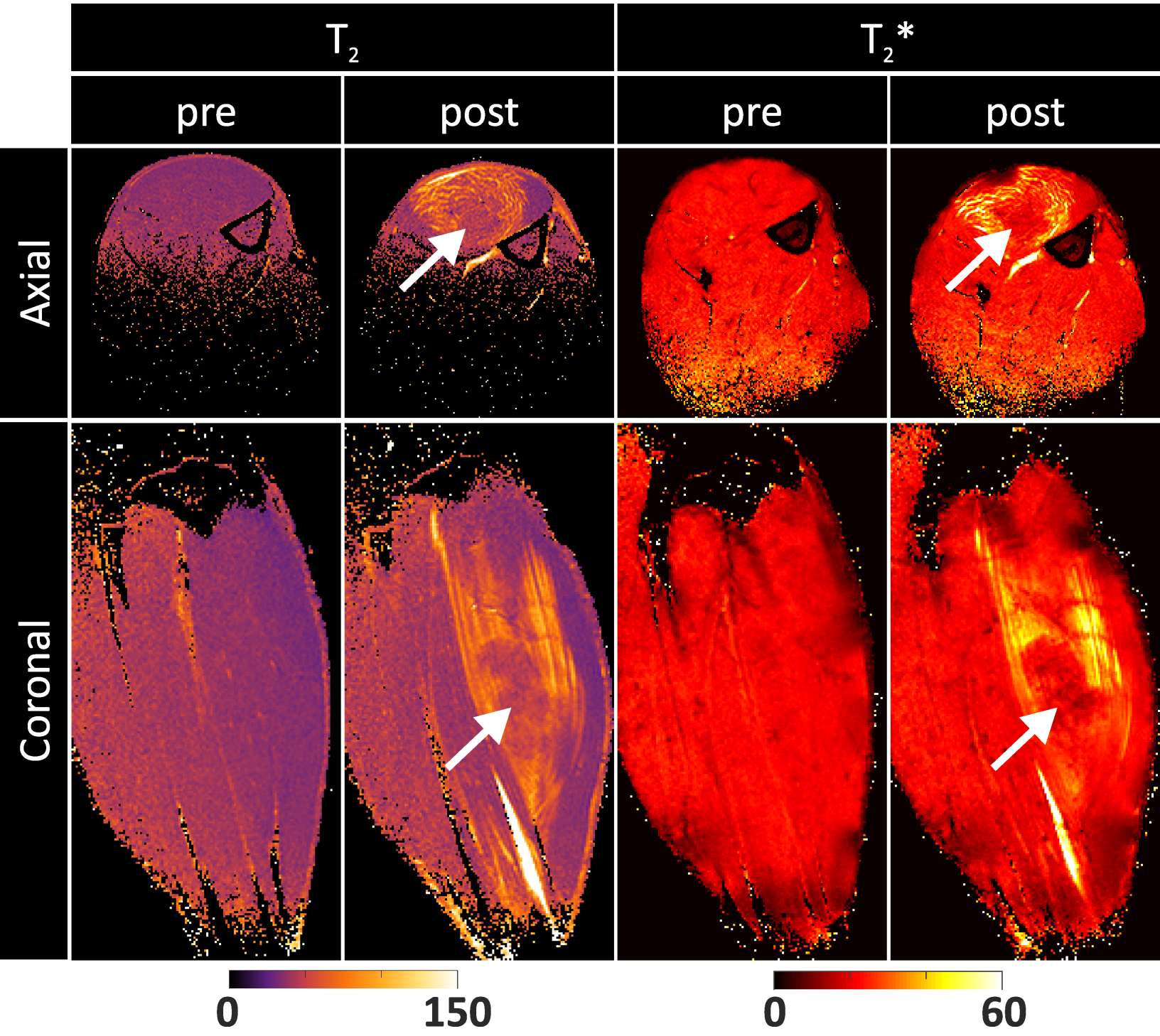
T2
T2*
pre
post
pre
post
Axial
Coronal
0
150
0
60

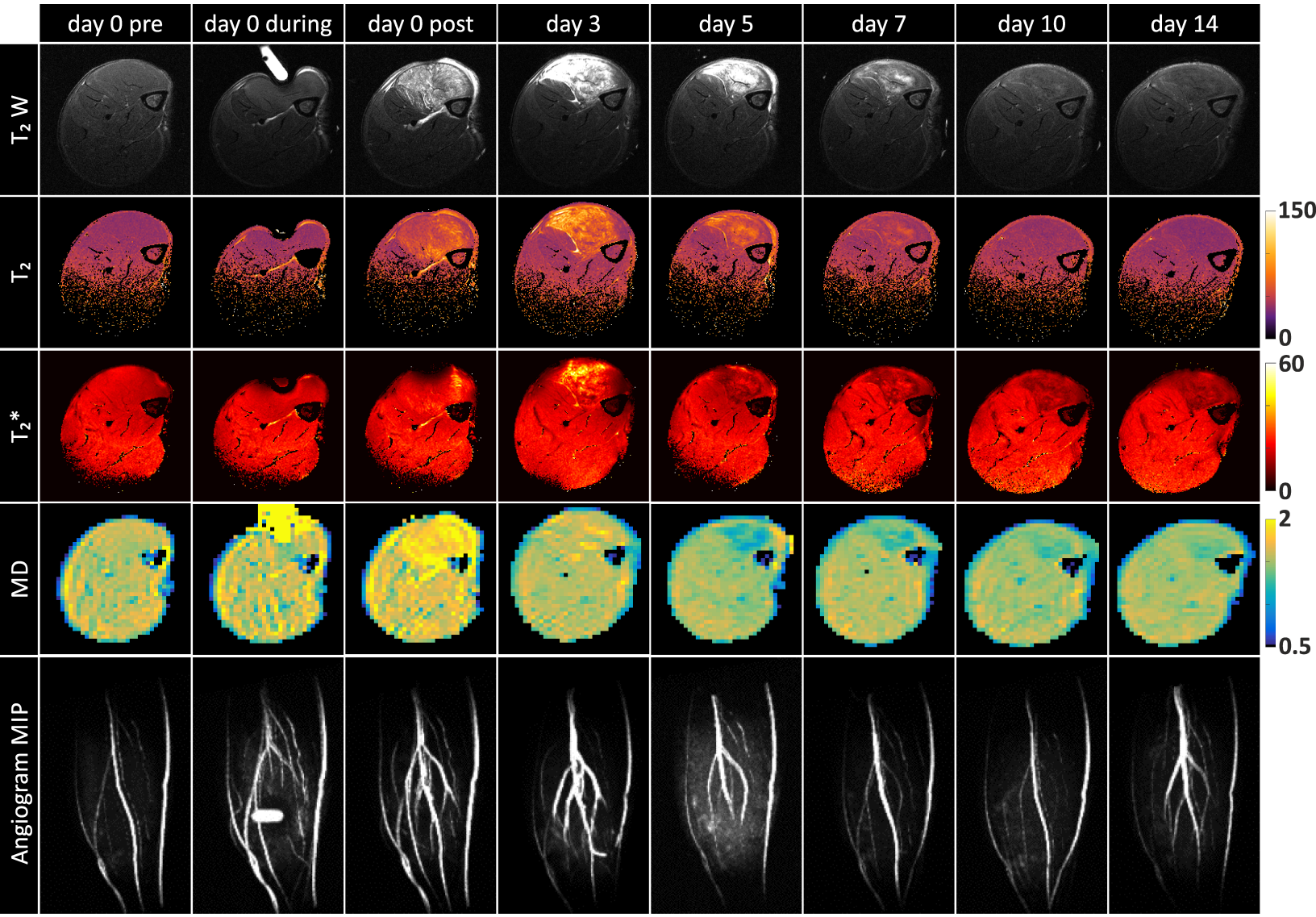
day 0 pre
day 0 during
day 0 post
day 3
day 5
day 7
day 10
day 14
T2 W
T2
T2*
MD
Angiogram MIP
150
0
60
0
2
0.5

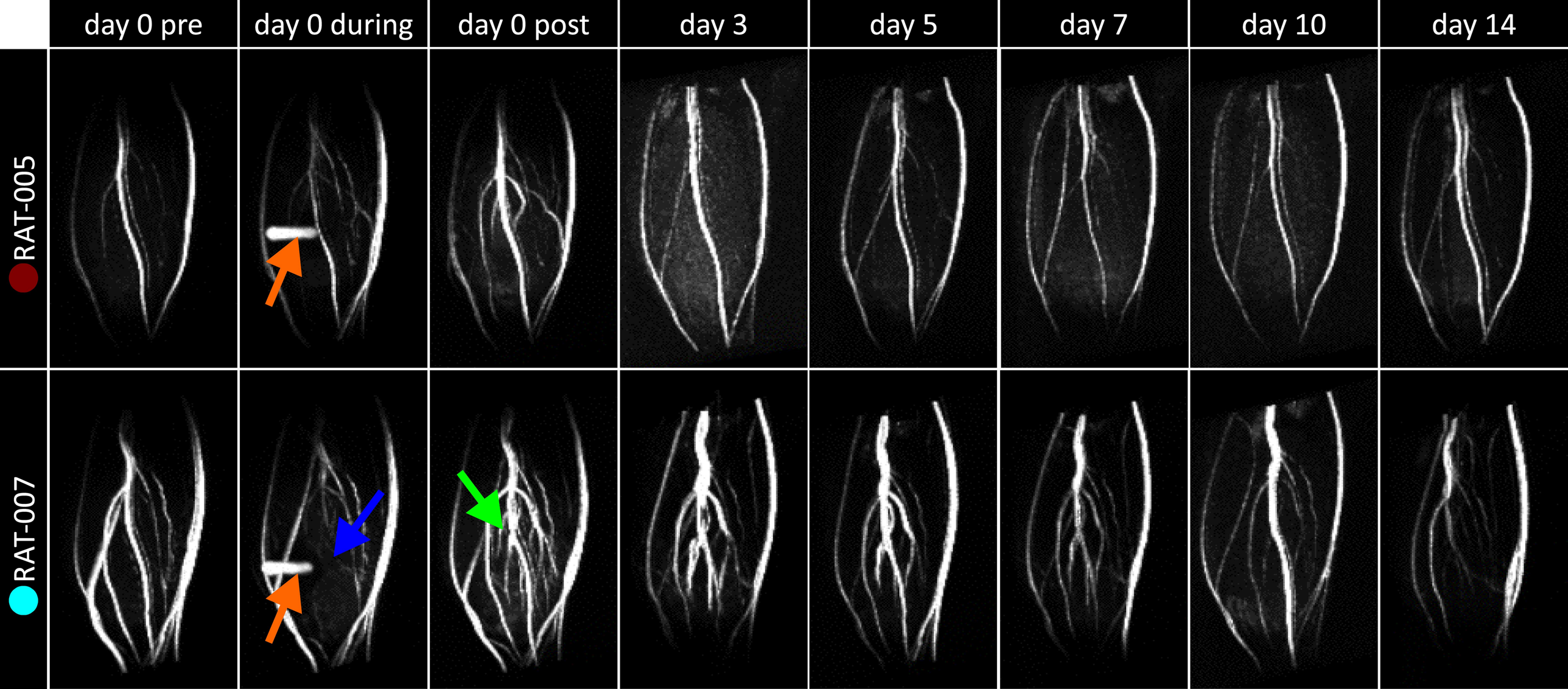
day 0 pre
day 0 during
day 0 post
day 3
day 5
day 7
day 10
day 14
RAT-005
RAT-007

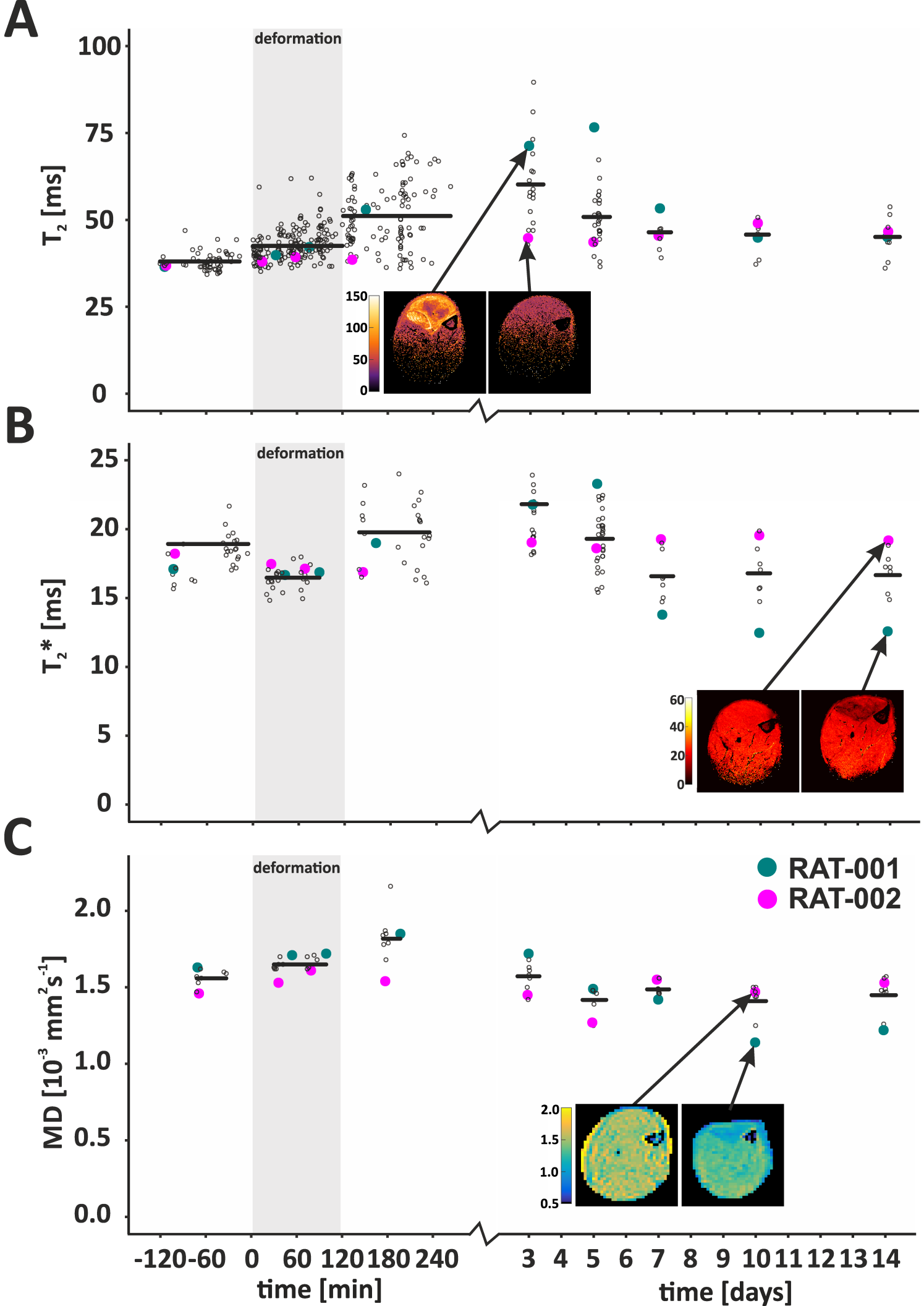
A
B
C
deformation
T_2 [ms]
T_2* [ms]
MD [10^{-3} mm^{2}s^{-1}]
RAT-001
RAT-002
time [min]
time [days]
-120 -60 0 60 120 180 240
3 4 5 6 7 8 9 10 11 12 13 14

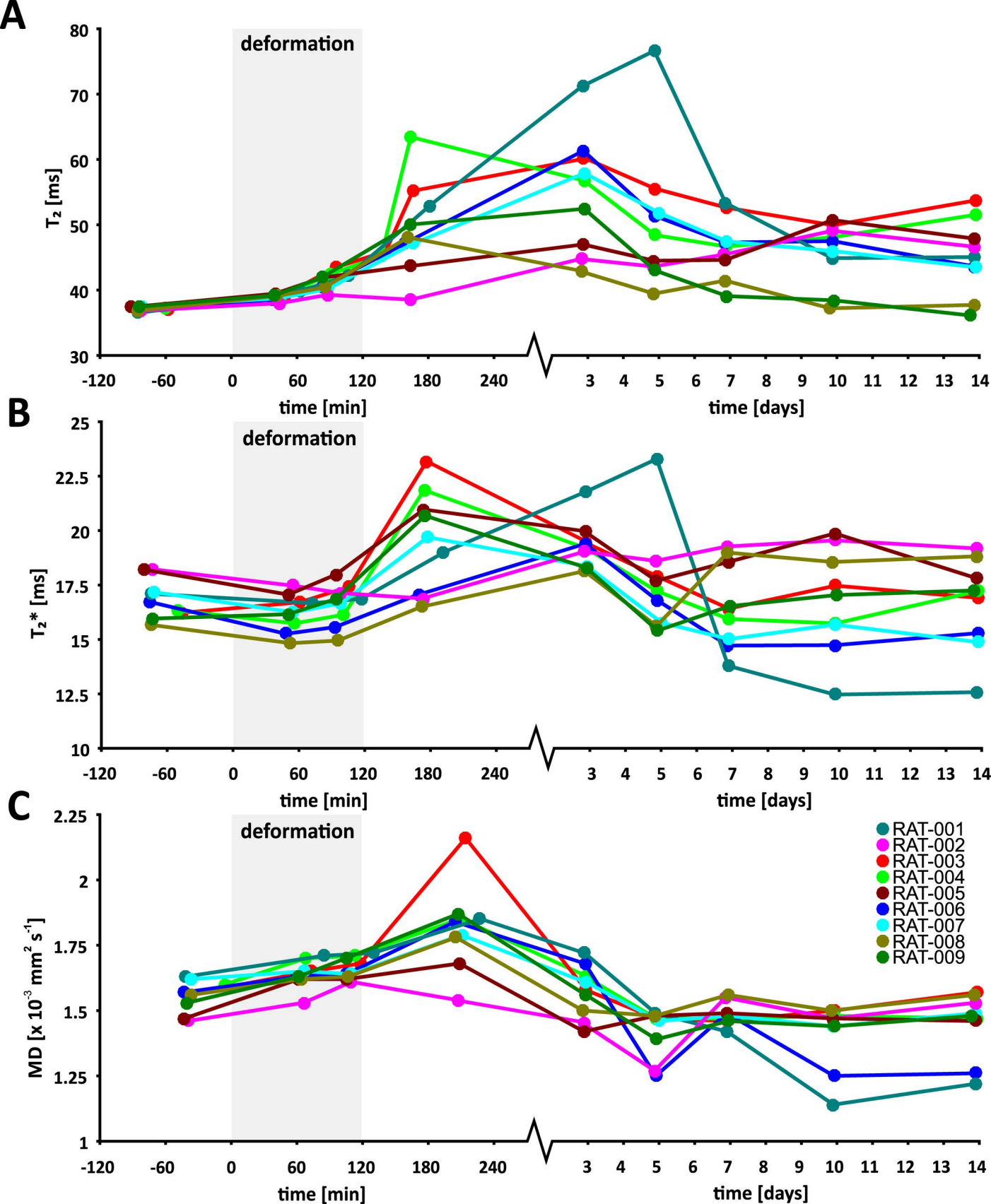
A
deformation
T2 [ms]
80
70
60
50
40
30
-120
-60
0
60
120
180
240
3
4
5
6
7
8
9
10
11
12
13
14
time [min]
time [days]
B
deformation
T2* [ms]
25
22.5
20
17.5
15
12.5
10
time [min]
time [days]
C
deformation
MD [x 10-3 mm2 s-1]
2.25
2
1.75
1.5
1.25
1
time [min]
time [days]
RAT-001
RAT-002
RAT-003
RAT-004
RAT-005
RAT-006
RAT-007
RAT-008
RAT-009

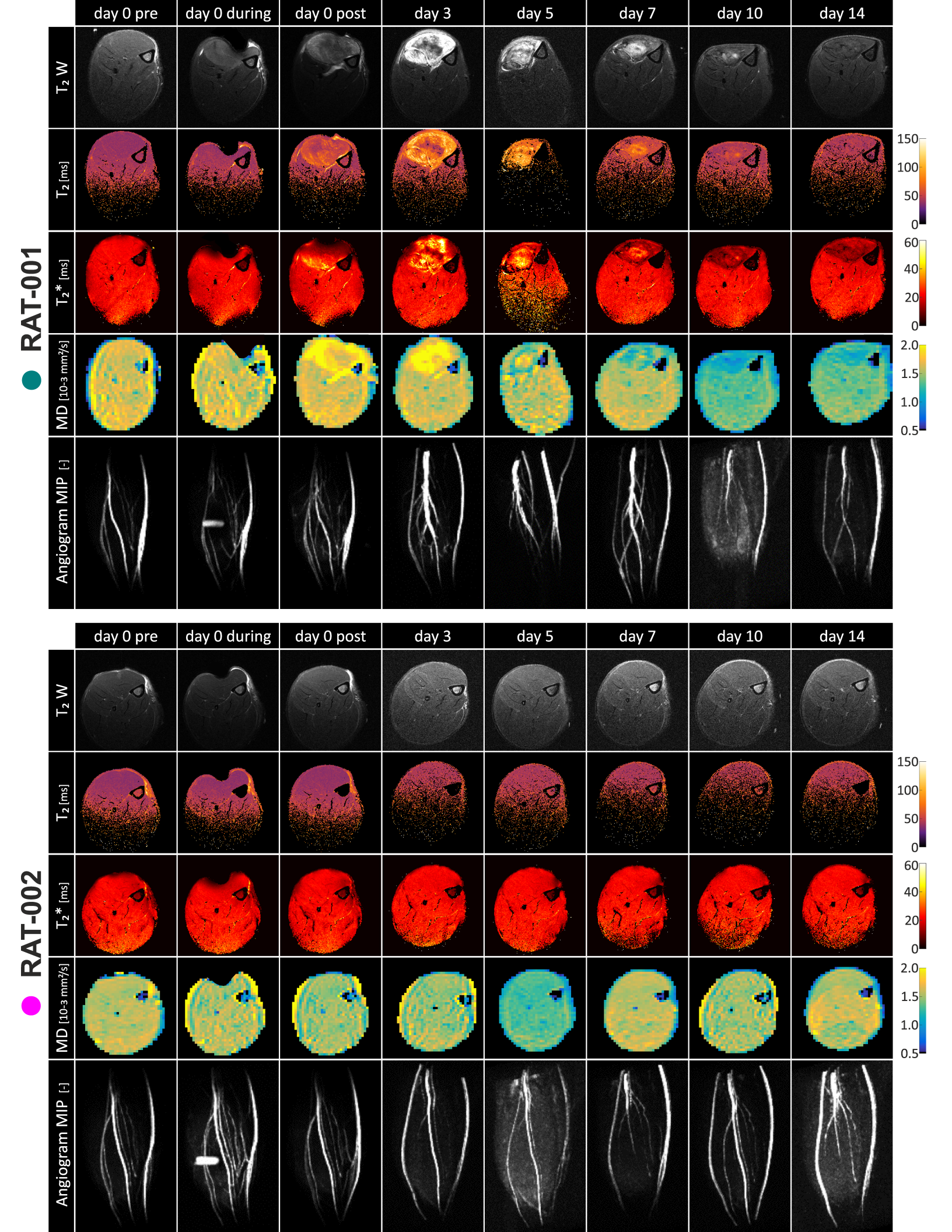
day 0 pre
day 0 during
day 0 post
day 3
day 5
day 7
day 10
day 14
RAT-001
RAT-002
T2 W
T2 [ms]
T2* [ms]
MD [10-3 mm2/s]
Angiogram MIP [-]
150
100
50
0
60
40
20
0
2.0
1.5
1.0
0.5

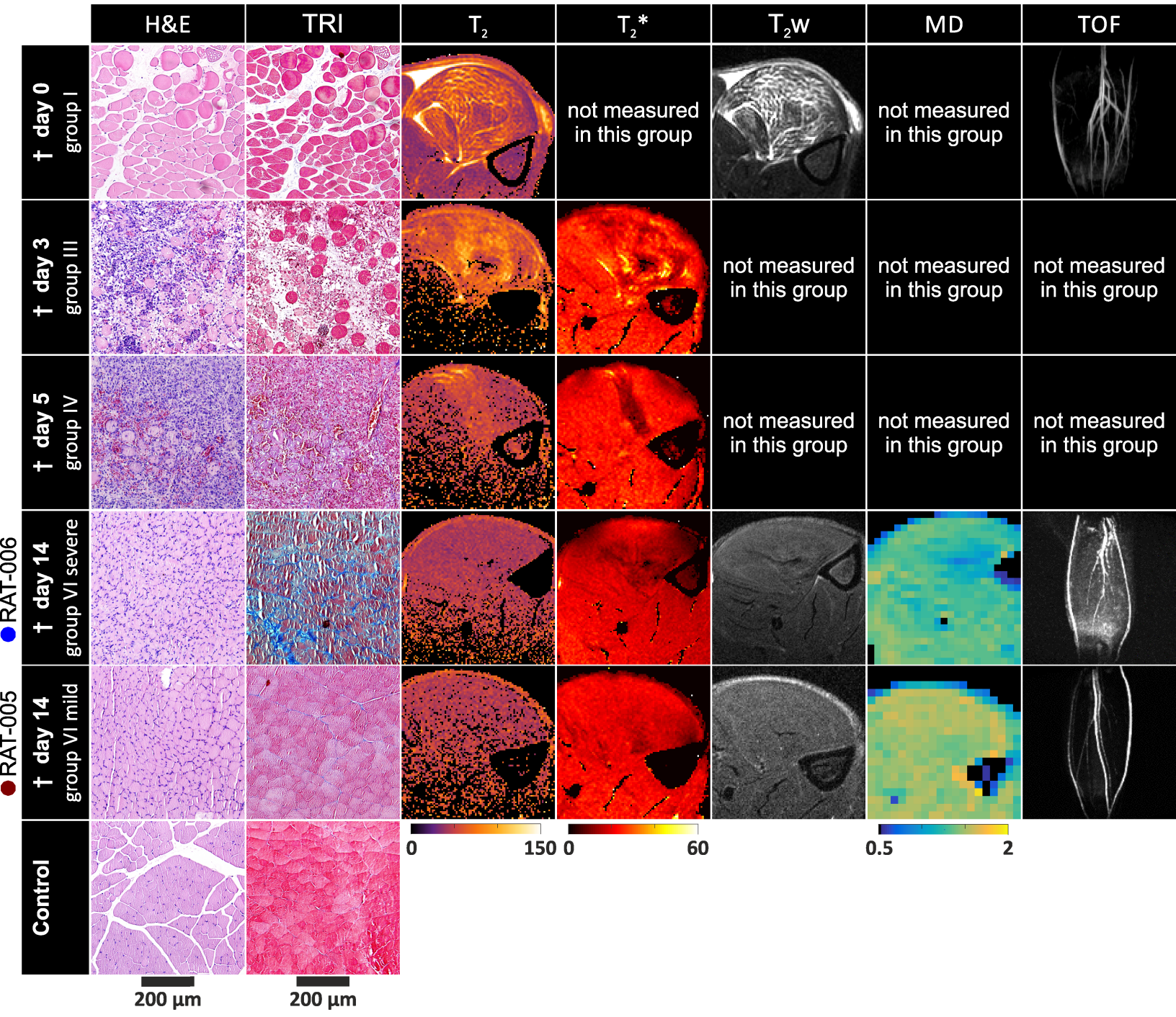
H&E
TRI
T2
T2*
T2w
MD
TOF
† day 0
group I
not measured in this group
not measured in this group
† day 3
group III
not measured in this group
not measured in this group
not measured in this group
† day 5
group IV
not measured in this group
not measured in this group
not measured in this group
† day 14
group VI severe
RAT-006
† day 14
group VI mild
RAT-005
Control
0
150
0
60
0.5
2
200 µm
200 µm

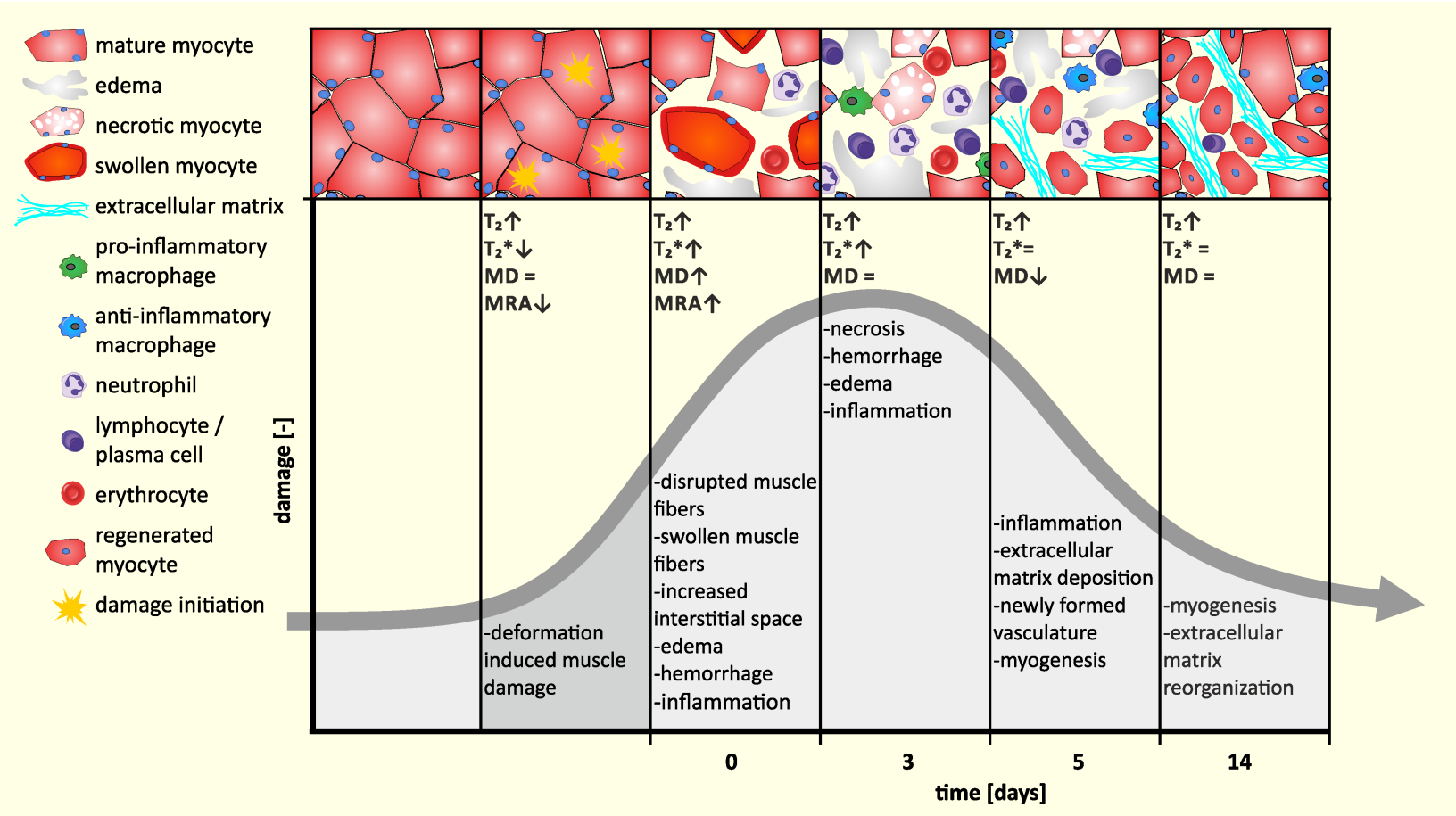
mature myocyte
edema
necrotic myocyte
swollen myocyte
extracellular matrix
pro-inflammatory macrophage
anti-inflammatory macrophage
neutrophil
lymphocyte / plasma cell
erythrocyte
regenerated myocyte
damage initiation
damage [-]
T₂↑ T₂*↓ MD = MRA↓
-deformation induced muscle damage
T₂↑ T₂*↑ MD↑ MRA↑
-disrupted muscle fibers
-swollen muscle fibers
-increased interstitial space
-edema
-hemorrhage
-inflammation
T₂↑ T₂*↑ MD =
-necrosis
-hemorrhage
-edema
-inflammation
T₂↑ T₂*= MD↓
-inflammation
-extracellular matrix deposition
-newly formed vasculature
-myogenesis
T₂↑ T₂* = MD =
-myogenesis
-extracellular matrix reorganization
0
3
5
14
time [days]

groups	time points[#]								rats	histology	MRI protocol[##]
group I	day 0 pre	day 0 during	day 0 post						n = 9 (SD) n = 6 (BN)	n = 4 (SD) n = 4 (BN)	T_2, TOF, T_2w,
group II	day 0 pre	day 0 during	day 0 post						n = 5	n = 4	T_2
group III	day 0 pre	day 0 during	day 0 post	day 3					n = 6	n = 4	T_2, T_2*
group IV	day 0 pre	day 0 during	day 0 post	day 3	day 5				n = 5	n = 4	T_2, T_2*
group V	day 0 pre	day 0 during	day 0 post		day 5				n = 19		T_2, TOF, T_2w, T_2*
group VI	day 0 pre	day 0 during	day 0 post	day 3	day 5	day 7	day 10	day 14	n = 9	n = 4	T_2, TOF, T_2w, T_2*, MD

	day 0 Pre	day 0 during 1	day 0 during 2	day 0 post	day 3	day 5	day 7	day 10	day 14
T_2 [ms] *all days (n = 9)*	37.0 ± 0.4	39.0 ± 0.5**	41.4 ± 1.4***	49.6 ± 7.1***	54.9 ± 9.2***	50.5 ± 11.1***	46.4 ± 4.6***	45.8 ± 4.9**	45.1 ± 5.8**
T_2* [ms] *all days (n = 9)*	16.8 ± 0.9	16.5 ± 0.9	-	19.5 ± 2.4*	19.3 ± 1.1*	17.6 ± 2.4	16.6 ± 2.0	16.8 ± 2.4	16.7 ± 2.1
MD [10^{-3} mm^2/s] *all days (n = 9)*	1.56 ± 0.06	1.64 ± 0.05	1.66 ± 0.04	1.82 ± 0.17***	1.57 ± 0.10	1.42 ± 0.09*	1.49 ± 0.04	1.41 ± 0.13*	1.45 ± 0.12
T_2 [ms] *day 0 only (n = 42)*	38.0 ± 2.3	40.2 ± 4.0***	44.6 ± 5.2***	51.5 ± 10.0***					
T_2* [ms] *day 0 only (n = 16)*	17.4 ± 1.0	16.6 ± 0.8*	-	19.5 ± 3.7					

muscle pathology	control (n = 24)	day 0 (n = 12)	day 3 (n = 4)	day 5 (n = 4)	day 14 (n = 4)
degeneration					
area of slide	1	2.3 ± 1.1**	3.5 ± 1.0*	3.3 ± 0.5*	1.3 ± 0.5
Severity	min	min-mld	mod-sev	mod-sev	min
necrosis	0	0.5 ± 0.7*	2.5 ± 1.0*	1.5 ± 0.6*	0
edema	0	1.5 ± 1.1**	3.0 ± 1.4*	1.8 ± 0.5*	0
hemorrhage	0	0.8 ± 0.8**	3.0 ± 1.4*	2.0 ± 0.8*	0
fibrosis	0	0.1 ± 0.3	0.3 ± 0.5	2.0 ± 0.8*	1.8 ± 0.5*
inflammation					
neutrophils	0	1.4 ± 1.2**	2.8 ± 1.5*	1.3 ± 0.5*	0
macrophages	0	0.3 ± 0.5*	2.3 ± 1.0*	3.3 ± 1.0**	1.0 ± 0.8*
lymphocytes/plasma cells	0	0.3 ± 0.5*	3.0 ± 1.4*	2.0 ± 0.8*	0.5 ± 0.6

	T_2 (n = 24) ρ	T_2^* (n = 10) ρ	MD (n = 4) ρ
degeneration			
area of slide	0.81***	0.78***	-0.17
necrosis	0.70***	0.82***	
edema	0.81***	0.82***	
hemorhage	0.78***	0.80***	
fibrosis	0.43*	0.03	-0.58
inflammation			
neutrophils	0.80***	0.80***	
macrophages	0.69***	0.57	-0.49
lymphocytes/plasma cells	0.62***	0.67*	-0.57